Master's thesis

NTNU
Norwegian University of Science and Technology
Faculty of Natural Sciences
Department of Materials Science and Engineering

Amirhossein Hojatshamami

Ni-Co and Ni-Fe Catalysts for The Oxygen Evolution Reaction in Alkaline Water Electrolysis

Master's thesis in MSCHEM
Supervisor: Frode Seland
Co-supervisor: Alaa Faid
October 2022

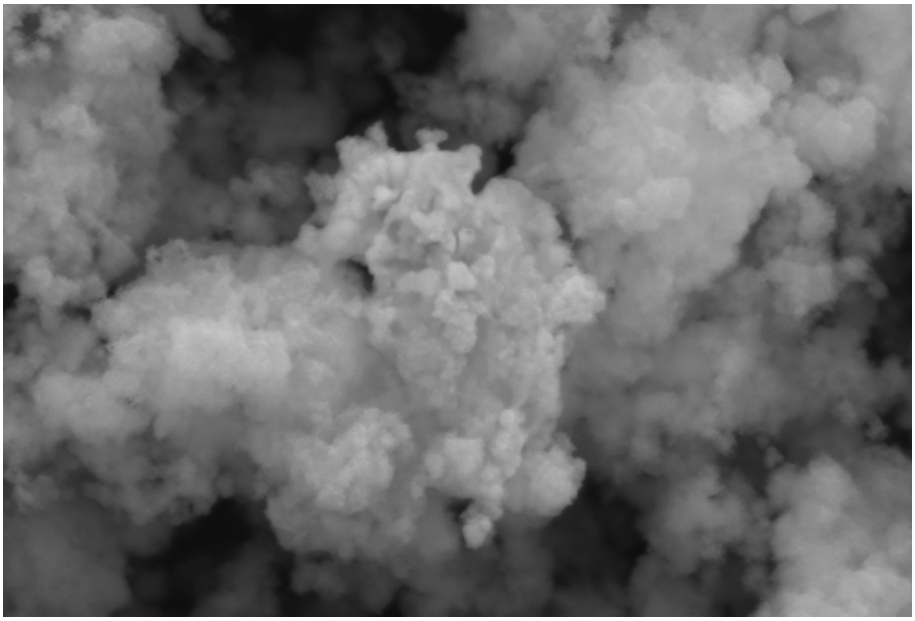

NTNU
Norwegian University of
Science and Technology

Amirhossein Hojatshamami

Ni-Co and Ni-Fe Catalysts for The Oxygen Evolution Reaction in Alkaline Water Electrolysis

Master's thesis in MSCHEM
Supervisor: Frode Seland
Co-supervisor: Alaa Faid
October 2022

Norwegian University of Science and Technology
Faculty of Natural Sciences
Department of Materials Science and Engineering

NTNU
Norwegian University of
Science and Technology

Abstract

Nickel-based catalysts were chosen for alkaline electrolysis of water due to their higher corrosion resistance and activity in alkaline environments. Alkaline membrane water electrolysis tries to combine the low cost of alkaline electrolysis with the high power and flexibility of PEM electrolyzers.

Nickel and its alloys make active, inexpensive, durable OER catalysts. Reducing an aqueous mixture of metal precursors with sodium borohydride produced Ni_xCo_y, Ni_xFe_y, and Ni. To ensure reproducibility, each experiment was repeated three times.

SEM was employed in addition to EDX to investigate the surface morphology and elemental composition of the produced nickel-based catalysts. XRD was used to examine nanoparticle phase purity and crystal formation.

The XRD results agreed with the BJH and BET surface-area studies, which found a correlation between surface area and crystallite size.

Ni_1Fe_3 has shown a bigger surface area than Ni_1Co_3. The Ni_1Fe_3 sample's porous surface may be the reason.

According to the LSV, the most promising catalyst is the Ni_1Co_3 catalyst, and both Ni_1Co_3 and Ni_1Co_1 accelerate OER. Metallic Ni offers quick electron transit within the nanoparticle, which is essential for catalysis.

In this study, the ECSA and RF of these catalysts were calculated. The RF value offers insight into the topology and distribution of active sites. RF greater than 1 indicates a larger and more favorable absorption area. This research shows that all catalysts with RF values above one have favorable adsorption surface areas.

Ni_1Co_3 and Ni_3Co_1 were the best electrochemical catalysts tested. These catalysts provide a larger, more favorable adsorption area than the others evaluated.

During OER, Ni_1Co_3 had the highest ECSA and RF values, which means that it forms the surface that lasts the longest.

These discoveries, along with the fact that the compounds are easy to make, using abundant raw materials, and can have their catalytic efficiency fine-tuned, make them good candidates for use in energy-related applications.

Preface

I would like to express my gratitude to Professor Frode Seland, my master's thesis advisor and the person who first introduced me to the field of electrochemistry, for providing me with excellent guidance during the entirety of this project.

Throughout this entire time period, your limitless knowledge and insightful thoughts have been quite helpful.

My co-supervisor, Alaa Faid, also deserves a very big thank you for all of his help. I am grateful to you for providing me with process solutions, which I used for measurements, and for aiding me in better comprehending the electrochemical aspect of the matter.

In addition, I would like to extend my gratitude to each and every knowledgeable, helpful, and kind individual who works at IMA. You all have been extremely helpful in teaching me a variety of experimental methods and technical instruments, and you have also contributed to wholesome conversations during this ongoing global pandemic.

In conclusion, I would want to express my gratitude to my close friends and family members for their unwavering support throughout the entirety of my academic life.

Table of contents

Chapter 1

Introduction

1.1. Background

Due to the increase in the world population, it is predicted that the world's annual energy consumption will double by 2050 and triple by 2100, according to human needs [1]. This increase in energy consumption, which is the result of global population growth, has created the main challenge of the present century, which is to find sustainable energy sources for the development of today's and tomorrow's generations. Throughout history, humans have always used the energy stored in high-energy molecules to supply the energy they need. These energy sources include wood and coal (biofuels) and, after the Industrial Revolution, oil, coal, and natural gas (fossil fuels). It is estimated that fossil fuels can supply the world's energy needs for many years to come. Nevertheless, environmental pollution, economic contexts, and security concerns have led to a reconsideration of the use of these resources. The use of these resources has led to the highest level of carbon dioxide in the atmosphere in the last 650,000 years [2]. If greenhouse gas emissions continue at the same rate, the world average temperature will rise by 3 to 5°C by 2100 [1].

Due to the increasing dependence on fossil fuels along with the reduction of reserves of their primary sources, research on new energy sources is of particular importance. Over the years, industries have experienced rapid growth, and the problems caused by global warming have intensified. In addition, the drastic reduction of fossil fuel resources has created a situation where the use of new technologies is necessary to reduce pollutant gases and increase the efficiency of energy-consuming systems. Today, it is important to find cheap and sustainable ways to obtain clean fuel, without or with a minimum release of greenhouse gases in the production and use of the fuel. Hydrogen is forecasted to be such a fuel. Hydrogen can be produced from water electrolysis using renewable energy sources and thus represents a sustainable and carbon neutral alternative. In water electrolysis, a direct electric current is applied between two electrodes in an aqueous electrolyte [3] where water is then decomposed into its constituent elements, oxygen at the anode, and hydrogen at the cathode. Demand for electrolytic-grade hydrogen is on the rise due to several factors, including the rise of hydrogen fuel-cell vehicles, the development of smart-grid energy flexibility, and the need to store energy

generated from renewable and nuclear sources. The high combustion temperature of a mixture of oxygen, hydrogen, and acetylene makes it possible to use this mixture in the welding and cutting industries. Electrolysis accounts for about 5% of global hydrogen gas production. Hydrogen is currently produced from natural gas through the steam reforming process in most industrial processes. The majority of electrolysis' hydrogen output is a byproduct of the manufacturing of chlorine and caustic soda.

Since electrolysis of water uses renewable H_2O and produces only pure oxygen as a byproduct, it is one of the most capable methods for producing hydrogen. Electrolysis also makes use of DC power from renewable sources like the solar system, wind, and biomass. In the steel industry, pure oxygen as well as oxygen-enriched air are used to perform various reactions. Today, oxygen is widely used in the chemical, fire containment, mountaineering, aviation, and diving industries. Liquid oxygen is also used in rockets to oxidize fuel. In addition, vegetable oil production plants use hydrogen, which is the product of water electrolysis, to hydrogenate vegetable oil [4].

There is currently a strong desire to produce hydrogen on a large scale as a secondary energy carrier for industries. Due to the high storage potential, the possibility of transfer, and non-pollution of the environment, hydrogen is of particular importance. Today, hydrogen is mostly produced through the methane conversion process [5]. Such processes use non-renewable resources and produce greenhouse gases, so they are not a valuable way to produce hydrogen. As a result, the production of hydrogen through the separation of water molecules using thermochemical or electrolytic processes has attracted much attention [6]. Large-scale electrolysis of water powered by renewable energy sources is currently the only viable process for green hydrogen production in a modern, carbon-neutral society.

1.2. Motivation

Increasing demand for fossil fuels and the pollution caused by their consumption have raised environmental concerns. Limited fossil fuel resources have also led to extensive research to find environmentally friendly alternatives to fossil fuels. Hydrogen produced by water electrolysis using renewable energy sources represents a sustainable alternative to fossil fuels.

Hydrogen is produced on the cathode side and oxygen on the anode side of the electrolyzers [7, 8]. Iridium is the best catalyst for the oxygen evolution reaction, with its unparalleled combined activity and durability, and platinum is the best catalyst for hydrogen evolution.

However, the high price and scarcity of iridium pose a significant threat to GW installations of water electrolyzers [9].

Alkaline water electrolysis employs alkaline electrolyte or membranes and makes it possible to use cheaper materials than the acidic PEM systems due to the alkaline environment in these systems. Nickel and nickel-based alloys can be used in high pH electrolytes and offer much cheaper alternatives than the noble metals and metal oxides that must be used in the acidic PEM systems. The oxygen evolution is slow in both devices, but while the hydrogen evolution at the cathode is fast in acidic systems due to its easy production from protons, it adds a significant contribution to the overall cell voltage in alkaline systems.

Increasing the efficiency of the oxygen and hydrogen evolution reactions and reducing the required potential are among the most important issues in the field of hydrogen production. Efficiency is more than just current at a certain cell voltage. Cost is a major concern for both producer and end user, so in order to increase the efficiency of the water electrolyzers, active, stable and cheap electrocatalysts must be developed [10].

In general, significant electrical energy and the use of expensive and rare materials are required to perform water electrolysis, which in turn are currently impeding the mass-market introduction of hydrogen in most industrial sectors. Therefore, reducing the overpotentials and ohmic resistance in water electrolyzers while reducing the cost of the materials is essential for GW installation [11].

Platinum and platinum-base alloys are very good hydrogen and oxygen evolution reaction catalysts due to their low activation overpotential. However, the high price of noble metals and the availability of some materials such as iridium are not justifiable with the idea of low-cost hydrogen production. The challenge today is therefore to identify alternative electrocatalysts with high activity, stability, and low cost, such as nickel and cobalt [12]. Significant efforts have been made recently to develop inexpensive and alternative electrocatalysts for platinum that hold critical properties such as low overpotential, high current density, high conductivity, stability in the operating environment, and availability. Therefore, researchers have focused on developing new platinum-substituted electrocatalysts with lower cost, more stability, and greater activity. Some transition metals and their alloys show comparable or even better electrocatalytic activity than platinum. In this context, nickel or nickel-based alloys or composites are promising catalyst materials to improve the electrocatalytic activity of the gas evolving reactions in alkaline water electrolysis [13].

1.3. Aim of work

In this study, Ni-based OER electrocatalysts were synthesized and the effects of adding Co and Fe to the Ni catalysts on the electrochemically active surface area, the intrinsic catalyst properties of the catalysts, and the efficiency of these catalysts for OER in alkaline systems were investigated. To put it another way, the purpose of this research is to find an answer to the question of which OER electrocatalysts are the most effective in increasing the efficiency of water splitting and are suitable replacements for noble metal catalysts.

An aqueous mixture of metal precursors is reduced in the presence of sodium borohydride in order to produce Ni_xCo_y, Ni_xFe_y, and Ni catalysts. Scanning electron microscopy, Energy-Dispersive X-ray spectroscopy, X-ray powder diffraction, BET, and BJH analysis were performed to physically characterize these catalysts, and for electrochemical characterization Electrochemical Impedance Spectroscopy, Linear Sweep Voltammetry, and Cyclic Voltammetry measurements were performed using a RDE setup to identify the properties of these catalysts and determine their effects on the efficiency of the oxygen evolution reaction.

Chapter 2

Literature and Theory

2.1 Hydrogen society and green economy

Widespread use of fossil fuels has led to greenhouse gas emissions and environmental damage [4]. Therefore, it is necessary to identify a cheap and clean fuel that has the potential to be carbon neutral. Hydrogen, as one of the simplest and most abundant elements in the world, can be produced without greenhouse gas emissions if produced from renewable energy sources. In recent years, hydrogen has been considered the energy carrier of the future with its high energy density and carbon-free combustion. It is predicted that hydrogen from water electrolysis combined with hydrogen storage and end-use (e.g. fuel cells) will be the dominating energy conversion in the coming centuries [5] and can alleviate the strong dependence on fossil fuels in modern societies.

Table 2-1 shows a comparison of the energy content of hydrogen and other fuels.

Table 2-1. Volume of different ways to store 1 kg of hydrogen equivalent [14].

	H_2 (kg)	Natural gas (Million m^3)	Raw oil (L)	Gasoline (L)	Petrol (L)
1 kg H2 ~	1	3.313	3.35	3.75	3.39

Hydrogen gas has a variety of applications in industrial units. Refineries, chemical plants, metal industries, and food industries use hydrogen gas in chemical processes. But the use of hydrogen is not limited to industrial units. Today, hydrogen is used as a source of clean energy to generate electricity in fuel cells and to power private cars or public transportation vehicles [15-17]. Today, hydrogen is mainly used in the production of ammonia, oil refining, and the manufacture of methanol. Hydrogen is also used in NASA's space program as fuel for spacecraft and in fuel cells that generate heat, electricity, and drinking water for astronauts [17-19]. Fuel cells are tools that convert hydrogen directly into electricity. In the future, hydrogen could be used as fuel for cars and airplanes, as well as to supply electricity to homes and offices [15].

One of the problems with the development and implementation of renewable energy is the need for energy storage in most of these systems. Solar thermal power plants and photovoltaic power plants are not capable of generating electricity overnight. On the other hand, the production capacity of wind farms decreases in some months of the year compared to other months [20].

The “duck curve” is a diagram showing electricity generation during a day that demonstrates the periodic imbalance between peak demand and the output of renewable energy. Such a diagram is provided in Fig. 2-1 during a sunny day in California. An important feature is illustrated by the orange graph, which climbs dramatically from 17:00 to 18:00 as the sun sets. As renewable energy output, specifically solar energy (grey curve), declines, there is a significant increase in demand for power generation from dispatchable sources (programmable, on-demand) to reach the market in one hour. The blue curve shows the demand for electrical power during the day. This concept was developed by Karen Edson in power generation on a utility-scale, California Independent System Operator [21, 22].

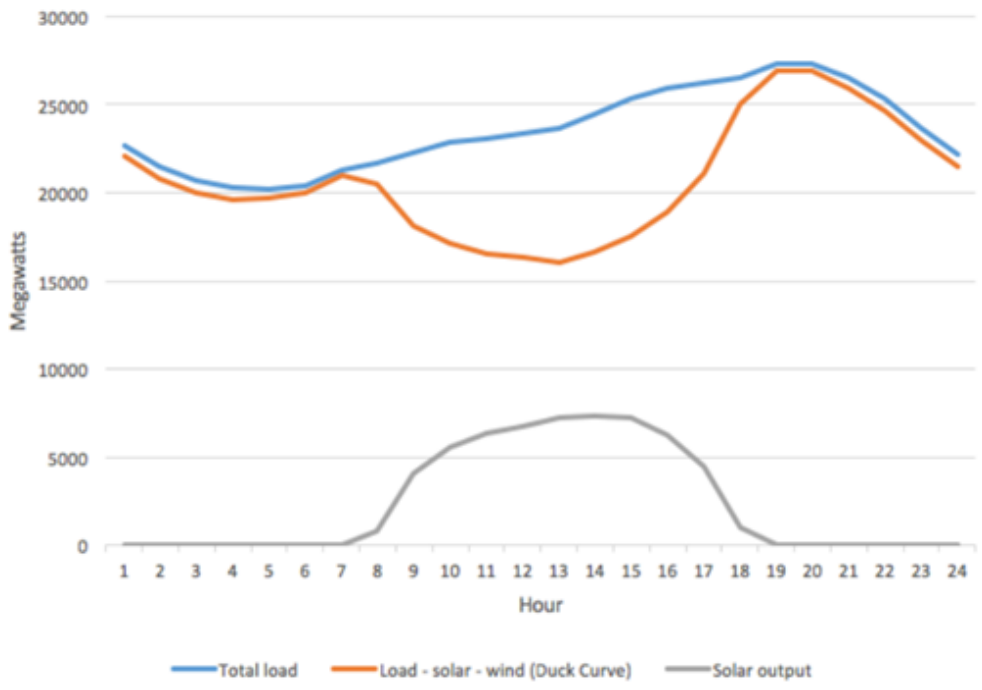

Fig. 2-1. The Duck Curve [21].

Following sundown when solar electricity is no longer accessible, high demand develops in many energy sectors. In the locations where a significant quantity of solar power has been deployed, the energy consumed from sources other than solar or wind shows a rapid increase in sundown and peaks at night hours, resulting in a graph similar to the side-view of a duck [22]. Other kinds of electricity generation must be rapidly expanded around the time of sunset,

after times of strong solar production, to make up for solar power losses. This is a key concern of grid operators with rapid photovoltaic growth [23]. Storage of energy can potentially solve these problems. Short-term usage of batteries can flatten the curve and sufficiently avoid fluctuations in the power generating system [24]. Cost is, however, one of the most important things to think about when storing energy, as this process is very expensive on a large scale.

One of hydrogen energy's main advantages is the capacity to store energy and provide power in winter as well as during the night for lengthy durations. This means that hydrogen may be used to overcome the challenges illustrated by the Californian duck curve by supplying electricity when the sun sets. Hydrogen has no capacity problems, as opposed to lithium ion batteries [25].

Hydrogen is the simplest element in the periodic table and, unlike fossil fuels, is a very light and small gaseous fuel (14 times lighter than air). At the same time, gaseous hydrogen has one of the highest heat capacities [26]. Table 2-2 summarizes some of the physical and chemical properties of hydrogen.

Table 2-2. Chemical and physical properties of hydrogen at standard temperature and pressure [27].

Parameter	Value
Name, symbol, number	Hydrogen, H, 1
Classification	Non-metal
Atomic mass	1.008
Number of electrons, protons, and neutrons	1, 1, 0
Color, smell	Colorless, odorless
State of matter	Gas
Density	Gas: 0.089 $g.cm^{-3}$, Liquid: 0.07 $g.L^{-1}$
Ionization energy	13.5989 eV
Liquid to gas expansion ratio	1:848
Melting point, boiling point	-259.14 °C, -252.87 °C
Low calorific value (LHV)	118.8 $MJ.kg^{-1}$
Burning temperature	2107 °C
Spark point	-253 °C

Unlike easily used fossil fuels, hydrogen does not exist freely in nature and is widely found in combination with oxygen and carbon. Therefore, the main challenge in hydrogen economics is the cost of energy that must be consumed in order to produce hydrogen. At present, the world's hydrogen production is about two million tons per day, which provides only 2% of the energy needs [26].

The main challenge in entering the hydrogen economy and replacing it with fossil fuels is the cost of producing this gas [28]. Hydrogen gas can be produced in a variety of ways and with a variety of sources, such as fossil fuels. Other sources of hydrogen include nuclear fuel, including thorium and uranium. In place of reforming hydrocarbons, nuclear reactors' excess energy could be used to produce electrolytic-grade hydrogen on a massive scale. Since the early 1970s, researchers have been working to perfect the concept of so-called "nuclear-hydrogen power" (the use of the energy generated by nuclear reactors for large-scale hydrogen production from water) and the wide application of this hydrogen in industrial, power-generating, transportation, and household needs [29]. Hydrogen can also be generated using geothermal sources; heat embedded in lava or hot underground rocks; and eventually solar, wind, or wave energy [30]. These energy sources can be classified into two groups: renewable and non-renewable. Renewable energy sources, such as wind or solar, do not emit environmentally hazardous materials and can produce energy sustainably. Non-renewable energy sources are a waste of resources and also harm the environment [25].

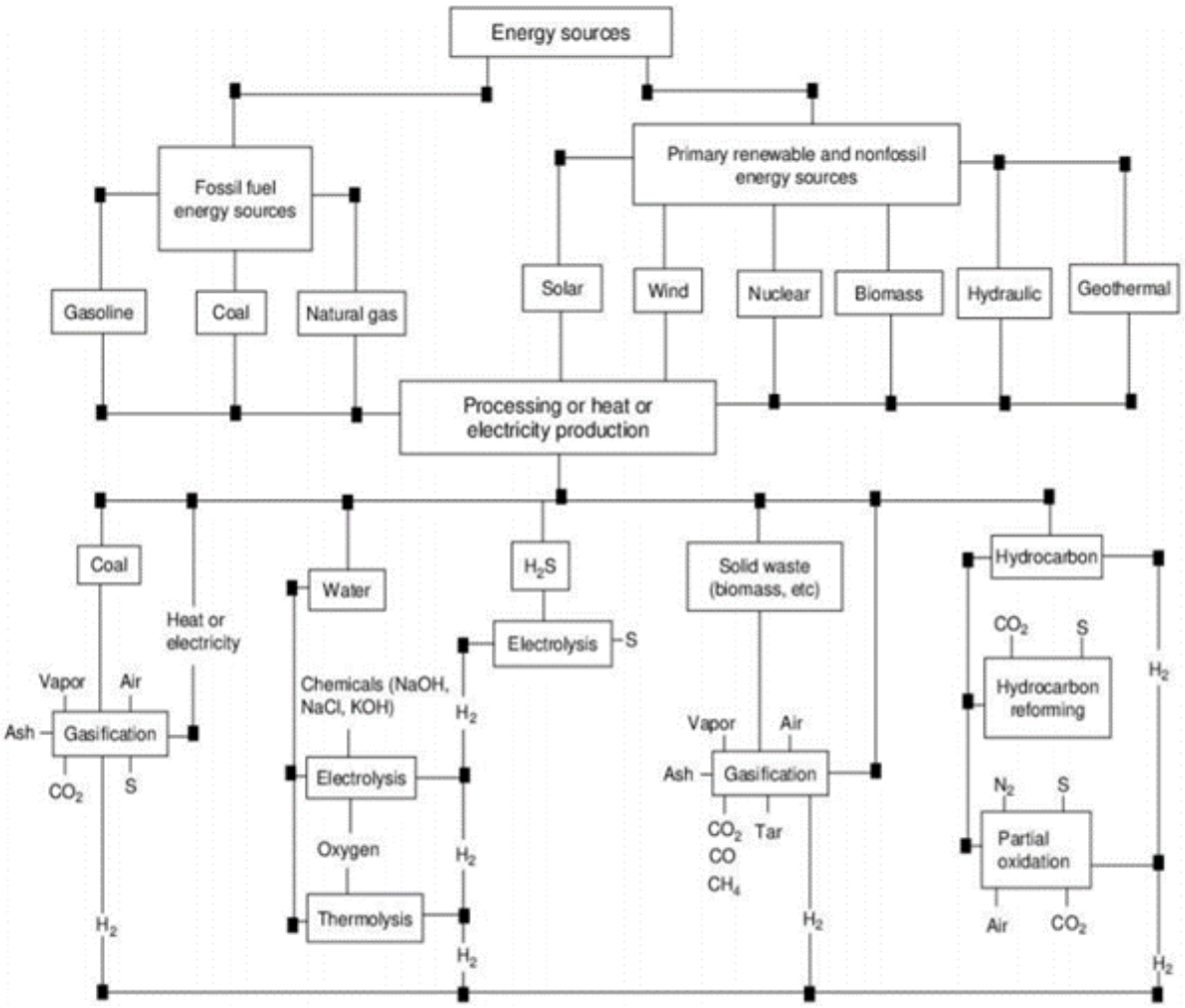

Fig. 2-2. Different methods of hydrogen production [30].

Among the various technologies and resources, the processes that use fossil fuels, biomass, and water to produce hydrogen are classified as major processes. As shown in Fig. 2-2, hydrogen can be produced from fossil fuels by the processes of natural gas vapor refining, natural gas heat loss, partial oxidation of heavy compounds (POX), or the conversion of coal to gas [31]. Hydrogen is also produced from biomass by the methods of incineration, pyrolysis, and gasification associated with liquefaction or biological production. Hydrogen can be produced from water as a raw material. Photolysis, thermochemical processes, thermolysis, and electrolysis, or even by connecting these processes by biological, thermal, and electrolytic methods, hydrogen can be produced [30]. The main step in the economical production of hydrogen is the use of sustainable, efficient, and environmentally friendly methods. The main challenge of hydrogen production methods is to reduce production costs. Cheap production will usher in a new era of hydrogen-based energy. Table 2-3 provides an overview of the costs of producing hydrogen in different ways.

Table 2-3. Costs of hydrogen production by different methods.

Method	Production cost (Euro/kg hydrogen)
Refining of light hydrocarbons [32]	1.06-2.08
Partial oxidation of heavy hydrocarbons [32]	0.72-1.41
Thermochemical conversion of biomass [33]	1.03-5.39
Photosynthetic microorganisms [34]	0.40-9.47
Photo-electrolysis of water [35]	1.07-13.5
Thermochemical cycles [36]	2.66-9.40
Alkaline and acid electrolysis [37]	1.94-8.60
High temperature electrolysis [38]	2.00-3.50

Factors influencing the costs associated with hydrogen production include [25]:

1- The amount of experience in using the relevant technology

2- Investment costs, implementation, maintenance, and replacement of various equipment

3- Product Manufacturing Scale

4- The cost of the resources used to produce the product

5- Efficiency, capacity, and lifespan of the production line

6- Purity of hydrogen produced

About 45 to 50 million tons of hydrogen are produced annually in the world. A large part of this amount is produced by refining methods of light hydrocarbons or oxidizing heavy hydrocarbons [39], as shown in Fig. 2-3.

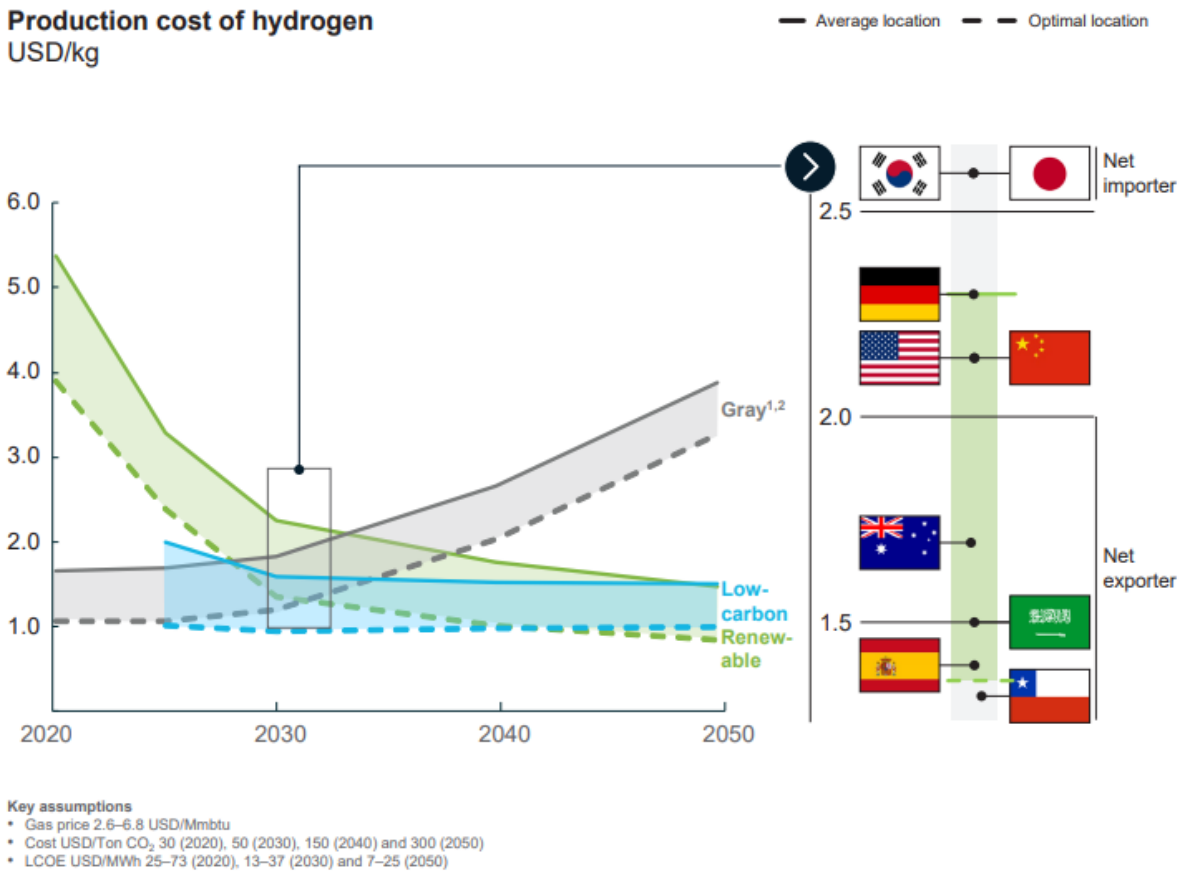

Fig. 2-3. Predicted cost of hydrogen production pathways [39].

Hydrogen produced by electrolysis accounts for about 4% of the world's hydrogen production, and the amount produced by other methods is very small and negligible. It is noteworthy that among all the various methods of hydrogen production, water electrolysis can be considered the most sustainable method of hydrogen production if the energy source used in this method is provided by renewable sources [40, 41].

2.2 Water electrolysis

Water electrolysis is one of the most important methods for producing hydrogen. Hydrogen and oxygen are produced from water by passing an electric current through it [5]. The hydrogen produced with this technology has a high purity and reaches up to 99.999% by volume. The purity of the hydrogen produced is one of the advantages of electrolysis. The hydrogen produced can be used directly in low-temperature fuel cells [5]. Depending on the size of the electrolyzer system, the price of hydrogen produced will vary from 3 to 5 euros per kilogram [39, 42]. Water electrolysis technologies include alkaline water electrolysis (AWE), anion

exchange membrane (AEM) water electrolysis, polymer electrolyte membrane (PEM) water electrolysis [43], and solid oxide water electrolysis [44].

Typically, large electrolyzer units are located next to hydroelectric power plants. To be able to take advantage of cheap electricity during off-peak hours. From an industrial point of view, the rate of development of alkaline electrolyzers is such that hydrogen can be produced at a suitable rate [45]. It should be noted that to produce hydrogen cheaply and competitively with other hydrogen production methods, larger production units are needed than what is currently available. Although PEM electrolyzers are commercially available, they are relatively expensive and are more suitable for small-scale hydrogen production [46, 47]. On the other hand, solid oxide type (SOE) electrolyzers, which produce hydrogen from water vapor, are still in the research phase. Since these types of electrolyzers operate at high temperatures, they consume less electricity and therefore have good potential for the production of cheap hydrogen [48]. SOE systems have a clear advantage when heat sources are available, like high-temperature nuclear reactors or concentrated solar power [45].

In water electrolysis, a direct current is applied between two electrodes in order to separate water molecules into oxygen and hydrogen. The two electrodes are in contact with an electrolyte that transports ions across but prevents electron transport and limits gas cross-over. The electrolyte could be either solid, such as in the PEM, AEM, or SOE systems, or an aqueous electrolyte, as in the AWE system. In all cases, the ionic conductivity is crucial, and a lot of research is devoted to improving the ionic conductivity while maintaining low gas cross-over and high durability [5]. Electrodes, on the other hand, must have good corrosion resistance, high electrical conductivity, good catalytic properties, and a strong, cohesive structure [49]. Electrodes, the electrolyte, and the diaphragm (separator or membrane) are the components that make up a water electrolyzer cell. The overall water electrolysis reaction for the liquid state is shown in Eq. 2-1 [3, 50].

$$H_2O \rightarrow H_2(g) + \frac{1}{2}O_2(g) \qquad \text{Eq. 2-1}$$

In the water electrolysis process, electrons are received or released at the electrode surface, commonly referred to as the electrochemically active surface area. Reactant water is supplied as liquid or gas to the catalytic sites. The resultant products, hydrogen, and oxygen are transported from the catalytic sites and collected separately at each electrode. Ions are transported in the electrolyte to maintain electro-neutrality at both the anode and the cathode during operation. In an AWE, hydroxide ions are transported from the cathode where they are

formed during hydrogen evolution from reduction of water to the anode where they are oxidized to form oxygen gas. Hydrogen is produced at the cathode and oxygen at the anode.

2.2.1 Thermodynamics

An electrolyzer is a device that converts electrical and thermal energy into chemical energy embedded in hydrogen [14]. The minimum electrical energy required to perform the splitting of one mole of water at a constant temperature and pressure by an electrolysis cell is the Gibbs energy change of the reaction (ΔG). The Gibbs energy is the reaction enthalpy (ΔH) of the electrolysis process subtracted from the reversible heat or heat energy (Q) equal to the process entropy (ΔS) multiplied by the reaction temperature (T). The electrolysis process is endothermic ($0 < \Delta H$) and non-spontaneous ($0 < \Delta G$).

$$\Delta G = \Delta H - Q = \Delta H - T\Delta S \qquad \text{Eq. 2-2}$$

The minimum potential required to perform an electrochemical reaction in a cell is called the reversible cell potential (V_{rev}). This potential is a function of ΔG and is defined as follows:

$$V_{rev} = -\frac{\Delta G}{zF} \qquad \text{Eq. 2-3}$$

In Eq. 2-3, z is the number of moles of electrons exchanged per mole of reaction (z = 2 per mole of hydrogen molecules produced). F is the Faraday constant and is equal to the charge of one mole of electrons (F = 96485 C/mol). If the thermal energy required for electrolysis ($T\Delta S$) is provided by electricity, the minimum potential required for this reaction is called thermo-neutral voltage (V_{tn}).

$$V_{\Delta H} = -\frac{\Delta H}{zF} \xrightarrow{ideal\ process} V_{tn} = V_{\Delta H} \qquad \text{Eq. 2-4}$$

In an ideal electrolysis reaction, V_{tn} would be equal to the enthalpy potential ($V_{\Delta H}$). However, in a real electrolysis process, V_{tn} will be larger than $V_{\Delta H}$. This difference is due to the consumption of excess energy (heat and electricity) resulting from irreversible thermodynamic losses.

At 298 Kelvin and one bar the thermodynamic variables of an electrolysis reaction will be as follows [16]:

ΔG°=237.21 kJ/mol

ΔS° =0.1631 kJ/mol

ΔH° =285.84 kJ/mol

By inserting the respective thermodynamic values into Equations 2-3 and 2-4, the thermo-neutral potential at standard states will be equal to 1.4811 *V* (from ΔH), while the reversible potential of water electrolysis from liquid water at standard states will be equal to 1.2291 V (from ΔG).

The energy consumption of an electrolysis reaction also depends on the temperature and pressure. Changing the magnitude of these two parameters will change the reversible and thermo-neutral potentials. Figures 2-4 and 2-5 show the energy consumption in kJ/mol of the electrolysis reaction as a function of temperature (298 to 1273 K) and pressure (1 to 100 atmospheres), respectively. Fig. 2-4 shows that the electrical energy required for the electrolysis (ΔG) reaction decreases with increasing temperature while the required heat ($T\Delta S$) increases. With water in liquid state, the total energy consumption (ΔH) decreases slowly as the temperature rises, while it increases slightly as vapor (above 100 °C). It is also important to note that at temperatures above 100 °C (373 K), the heat of vaporization of water (40.8 kJ/mol) must be added to the energy required for the reaction. At high temperatures, electricity consumption is significantly lower than at low temperatures. This is a key advantage of hydrogen production from water vapor in solid oxide electrolyzers operating at high temperatures [13].

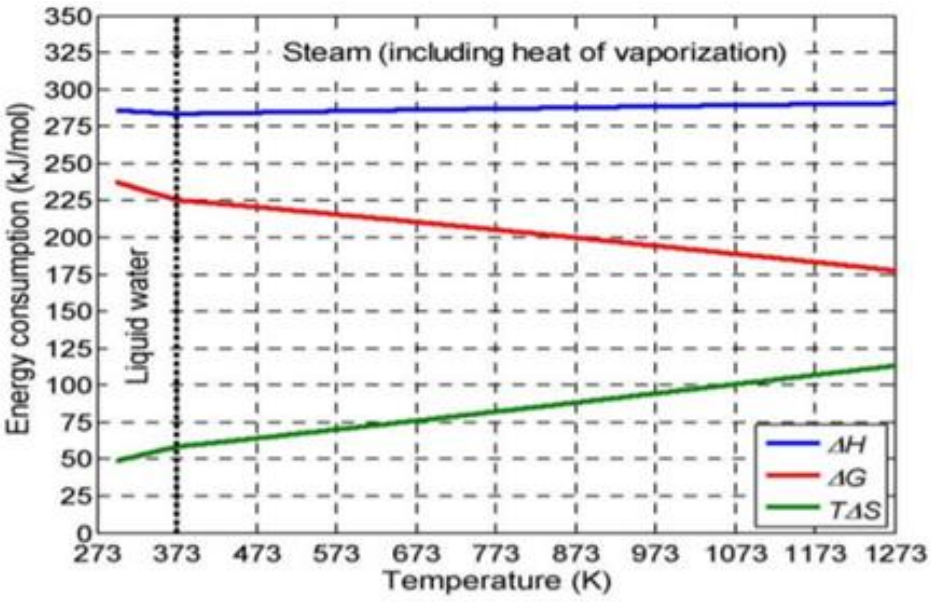

Fig. 2-4. Evaluation of energy consumption of an electrolysis reaction as a function of temperature at standard pressure (1 bar) [17].

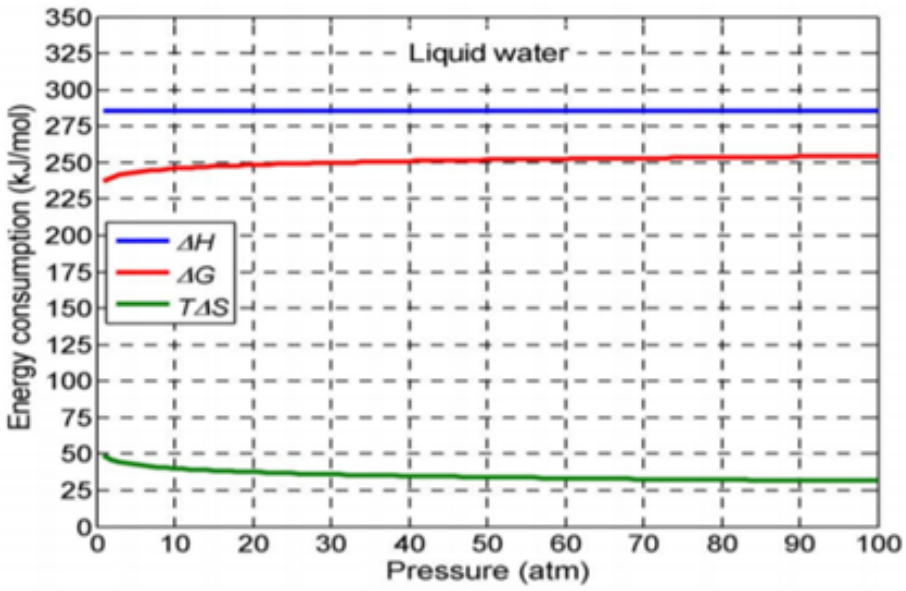

Fig. 2-5. Evaluation of energy consumption of water electrolysis from liquid water as a function of pressure at 298 K [17].

Figure 2-5 shows that the electrical energy consumption (ΔG) of water electrolysis from liquid water increases slightly with pressure due to the dependence of the reversible heat with pressure. The electrical energy consumption will increase by about 7.3% when the pressure increases from 1 atmosphere to 100 atmospheres. Although the consumption of electrical energy increases with increasing pressure, the heat consumption of the reaction ($T\Delta S$) will impose an identical decrease with the increasing pressure. As a result, the effect of an increasing electrical demand will be offset by a decreasing heat demand with increasing pressure. So, if we increase the pressure from 1 to 100 atmospheres, the energy consumption of the whole electrolysis process (ΔH) is independent of the pressure change and will remain constant.

2.2.2 Loss terms, energy consumption and efficiency

As a direct current is applied to produce hydrogen in an electrolyzer, the value of the cell voltage (V_{cell}) depends on the reversible potential (V_{rev}), the various irreversibilities (overpotentials), conductivity, and unwanted currents.

The cell voltage (V_{cell}) needed to provide a certain hydrogen production (i.e., current) is the sum of the reversible voltage and the necessary overvoltage (Eq. 2-5.).

$$V_{cell} = V_{rev} + V_{ohm} + V_{act} + V_{con} \qquad \text{Eq. 2-5}$$

The V_{ohm} parameter is ohmic overvoltage, which is primarily due to the resistance to the movement of ions through the electrolyte. The resistance of passing electrons through cell components (electrodes, current collectors, etc.) as well as constriction resistances also contribute to this overvoltage. The V_{ohm} parameter is proportional to the electric current used in the cell and is predominant at higher current densities (i.e., higher production rates). V_{act} is commonly referred to as the activation overvoltage and is related to the reaction kinetics at the electrodes. V_{act} is the sum of the activation overpotential at the anode (oxygen evolution) and at the cathode (hydrogen evolution) and is the voltage needed in order to transfer electrons across the electrode/electrolyte interface at a given current density. In general, this overvoltage depends on the catalytic properties of the electrode materials. The oxygen evolution at the anode is rather sluggish and requires, in general, a high activation overpotential to proceed. The hydrogen evolution at the cathode is a fast reaction in acidic systems due to the easy reduction of protons and therefore leads to a low activation overpotential in PEM systems. However, hydrogen evolution is a significantly slower process in alkaline systems and contributes considerably to the activation overvoltage. The activation overvoltage (V_{act}) has a non-linear and logarithmic behavior with respect to the current density applied to the cell [51].

V_{con} is commonly known as the concentration overvoltage and is generated by mass transfer processes. This limitation in transmission reduces the concentration of the reactants and increases the concentration of the products in the catalytic layer. Usually, the value of V_{con} is much less than the values of V_{act} and V_{ohm} but can be dominant at very high current densities and/or certain conditions (e.g., bubble trapping). This difference is much more pronounced in the case of alkaline electrolyzers. The relationship between cell voltage (V_{cell}) and current (I_{cell}) or a so-called *I-V* curve, is provided in Fig. 2-6.

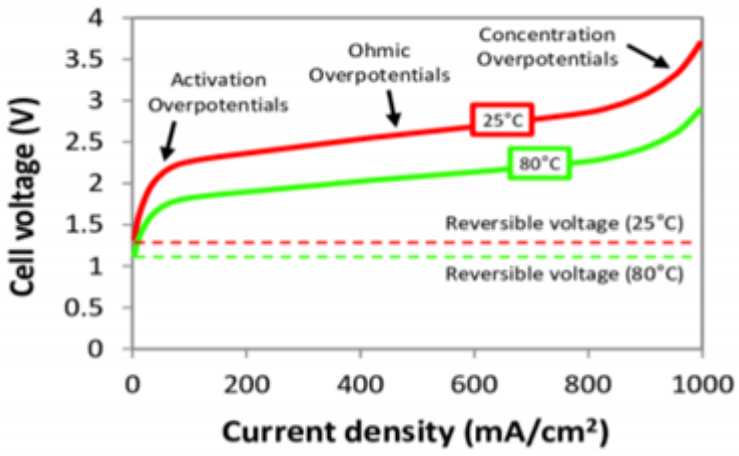

Fig. 2-6. *I-V* curves of an alkaline electrolysis cell at temperatures of 25 and 80°C [52].

The *I-V* curve depends on the operating conditions, and in particular on the temperature, as illustrated in Figure 2-6 for 80 and 25°C. At a constant current density, reversible, ohmic, and activation overvoltages decrease, with increasing temperature. As a result, the cell voltage will also decrease, and the system can generate more hydrogen at a given power consumption. On the other hand, pressure has a negligible effect on the *I-V* curve. To be able to compare cells with different surface areas, the *I-V* curve must be plotted in terms of current density. Initially, the curve increases logarithmically, but as the current increases, it will become linear. At low current densities, the effect of activation overvoltage is the dominant phenomenon. But at high current densities, the effect of ohmic and concentration overvoltages will be more pronounced.

According to Faraday's law, the rate of hydrogen production is proportional to the transferred charge, or electric current (I_{cell}). The rate of hydrogen production in Nm^3/hour can be estimated using Eq. 2-6.

$$f_{H_2=\eta_F \frac{N_{cell} I_{cell}}{zF} \frac{22.41}{1000} 3600} \qquad \text{Eq. 2-6}$$

In this equation, η_F is Faraday efficiency, N_{cell} is the number of cells that make up the electrolysis unit, and I_{cell} is the current applied in amperes. Faraday efficiency, also known as current efficiency, is the ratio between the ideal electric charge to produce a certain amount of hydrogen and the actual electric charge consumed by the electrolyzer unit for a certain number of cells. The Faraday efficiency is less than one because of the unwanted currents that appear in a real electrolytic cell and do not participate in hydrogen production, such as corrosion of electrode materials (catalyst and catalyst support, porous transport material or bipolar plates) and cross-over and subsequent reduction/oxidation of product oxygen/hydrogen [3, 53].

The energy used to produce hydrogen is called the specific energy consumption, C_E, and its unit is kWh/Nm^3. This parameter increases with an increase in the rate of hydrogen production [3]. The specific energy consumption for the electrolysis process is expressed in terms of time, *t*, and can be estimated using Eq. 2-7.

$$C_E = \frac{\int_0^{\Delta t} N_{cell} \cdot I_{cell} \cdot V_{cell} dt}{\int_0^{\Delta t} f_{H_2} dt} \qquad \text{Eq. 2-7}$$

Eq. 2-7 considers only the energy consumption of the electrolysis reaction and does not take into account the energy consumption of auxiliary hardware such as magnetic valves, pumps,

sensors, processors, the electrolyte cooling system, and purification units. The purification units are used to remove water vapor and oxygen from the hydrogen produced.

Finally, another important parameter for a water electrolysis cell is the cell efficiency, η_E. This parameter expresses the ratio between the energy contained in the hydrogen produced and the energy required to electrolyze the water used in the process. As a result, η_E can be obtained by dividing the high heating value (HHV) of hydrogen (3.28 kWh/Nm³) by the specific energy consumption of C_E, as shown in Eq. 2-8.

$$\eta_E = \frac{HHV\ of\ H_2}{C_E}.100 \qquad \text{Eq. 2-8}$$

The efficiency can be calculated for an electrolysis cell or any hydrogen generator.

2.2.3 Proton exchange membrane (PEM) water electrolyzer

A PEM electrolyzer consists of a proton conductive membrane, creating an acidic environment sandwiched between two electrodes where hydrogen evolution (cathode) and oxygen evolution (anode) occur. PEM electrolyzers employ noble metal catalysts such as ruthenium, rhodium, iridium, and platinum, and a perfluorinated sulfonic-acid membrane such as Nafion 117 as a proton conducting electrolyte. The Nafion membrane not only separates the electrodes and ensures ionic conductivity, but also plays a role in separating the gases. At the PEM electrolyzer anode, the water molecule is converted to protons and oxygen gas (Eq. 2-9). Protons are transported across the membrane to the cathode, where the protons are reduced to hydrogen gas. There is no need for a separating unit due to the solid membrane efficiently separating the gases. Depending on the required purity, a dryer is used to remove water. This electrolyzer has a low ionic resistance, leading to high efficiency and high operating current densities of about 1600 mA cm^{-2} in conventional systems and up to 4000 mA cm^{-2} in thin-membrane systems[76]. However, although very thin membranes lead to lower ohmic losses, they may also lead to considerable cross-over and a higher risk of membrane failure and thus a shorter lifetime. A schematic diagram of a PEM electrolyzer cell is shown in Figure 2-7. Anodic and cathodic reactions are according to Eq. 2-9 and Eq. 2-10 for the liquid state.

$$2H_2O \rightarrow O_2 + 4H^+ + 4e^- \qquad \text{Eq. 2-9}$$

$$4H^+ + 4e^- \rightarrow 2H_2 \qquad \text{E. 2-10}$$

The overall reaction for liquid state is identical to that of alkaline water electrolyzers and is in accordance with Eq. 2-11.

$$H_2O \rightarrow H_2 + \frac{1}{2}O_2 \quad \Delta H = 288\ \text{kJmol}^{-1} \qquad \text{Eq. 2-11}$$

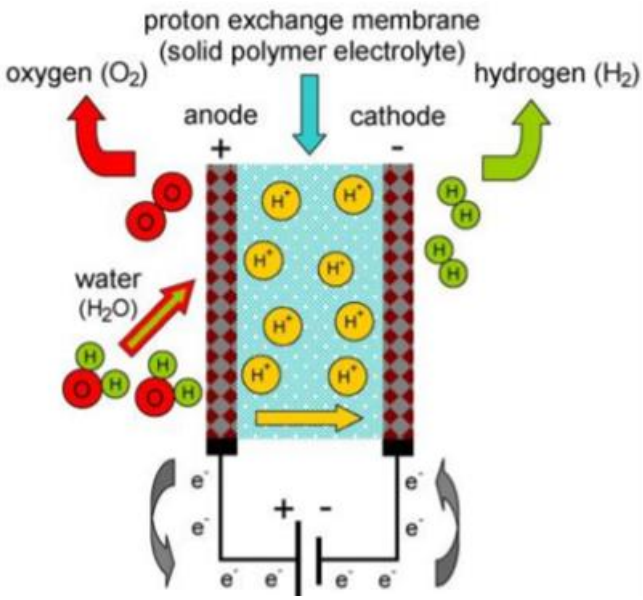

Fig. 2-7. Schematic of PEM electrolyzer cell [54].

2.2.4 Alkaline water electrolyzer

The electrolysis of alkaline water has a long history in the chemical sector. It is a kind of electrolyzer that is characterized by having two electrodes working in a potassium hydroxide (KOH) or sodium hydroxide liquid electrolyte solution (NaOH). The alkaline water electrolysis principle is straightforward. The direct current is delivered to the water, as stated in Eqs. 2-12, 2-13, and 2-14, and is used to split water into oxygen and hydrogen.

Cathode: $2H_2O + 2e^- \rightarrow 2OH^- + H_2$ Eq. 2-12

Anode: $2OH^- \rightarrow \frac{1}{2}O_2 + H_2O + 2e^-$ Eq. 2-13

Overall: $H_2O \rightarrow H_2 + \frac{1}{2}O_2$ Eq. 2-14

Such electrodes are divided into diaphragms, which separate the product gases from one element to the other, carrying the hydroxide ions (OH^-), as shown in Fig. 2-8. The latest comparison has shown that state-of-the-art nickel-based water electrolyzers with alkaline electrolytes have a competitive or even greater efficiency than platinum metal-based

electrocatalysts with acidified polymer membrane water electrolysis. Electrolysis needs the existence of a solution of minerals. Tap, well, and groundwater contain different minerals, some of them alkaline and others acidic. Alkaline water electrolysis might be seen as a key technique for efficient energy conversion and storage in the context of the decarbonization of industry.

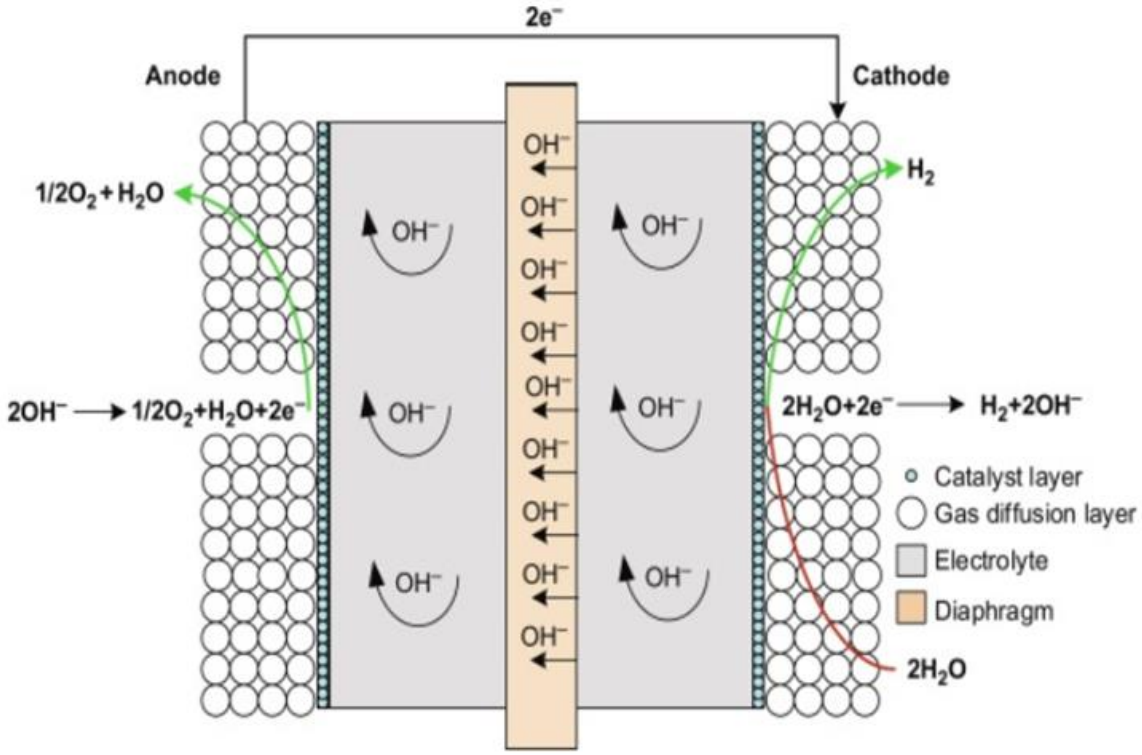

Fig. 2-8. Schematics of an alkaline water electrolyzer [54].

Typically, electrodes are separated by a thin, porous foil (from 0.050 to 0.5 mm in thickness), usually called a diaphragm or separation device. The ion-conductive diaphragm avoids electric shorts between the electrodes and allows tiny distances between the electrodes. The ionic conductivity is provided by the aqueous alkaline solution that enters the diaphragm pores. The cutting-edge diaphragm is Zirphon, zirconia, and polysulfone composite material. The diaphragm further avoids the mixing of the generated hydrogen and oxygen at the cathode and anode, respectively.

Noble metal catalysts such as iridium and ruthenium are very active catalysts. However, they are considered inappropriate alternatives as anode catalysts due to the very high price of the metal. Nickel-based metals are therefore commonly employed as electrodes in alkaline water

electrolysis. Ni is the most active non-noble metal catalyst material. and thought to be more stable during the development of oxygen.

A larger active surface area benefits the overall current at a given geometric surface area. A large surface area Ni catalyst may be made by dealloying Nickel-Zinc or Nickel-Aluminum alloys in alkaline electrolytes. This large surface area nickel material is also known as Raney nickel. Plasma vacuum sprayed Ni alloys on Ni meshes and hot dip galvanized Ni meshes were the highest performing electrodes in cell testing thus far reported [71]. Because it is inexpensive and easily scalable, the latter method may be appealing to large-scale industrial manufacturers. As nickel in itself has become a larger cost in AWE manufacturing, steel materials are considered a cheaper alternative to pure nickel electrodes. Significant efforts have been made lately to investigate the use of activated steel materials as replacements for bulk Ni electrodes [77].

2.2.5 Anion exchange membrane water electrolyzer

Anion exchange membrane electrolyzers typically consist of two electrodes; an anion-conducting membrane and an alkaline electrolyte solution, usually a 30% by weight solution of soda or potash to maintain the high ion conductivity of the membrane. In general, an ion-exchange membrane is constructed of organic or inorganic polymers containing ionic side groups, such as resins for ion exchange. Anion-exchange membranes include primarily mobile anion cationic groups; the most important factor in anion transport is anion conductivity, given that the anion is the dominating species.

Anion exchange membranes are typically coated with platinum as the cathode catalyst, and nickel or copper coated with metal oxides such as manganese, tungsten, or ruthenium are used as anode catalysts. The liquid electrolyte is not consumed in the reaction but must be replaced each time due to waste generated during the hydrogen production process. In an alkaline cell, the water molecule flows to the cathode, where water separates into H_2 and OH^-. OH^- travels through the electrolyte to the anode where O_2 is formed. The H_2 generated by the gas-liquid separator unit is sent out of the electrolyzer. Fig. 2-9 shows a schematic of an electrolyzer with an anion exchange membrane (OH^-).

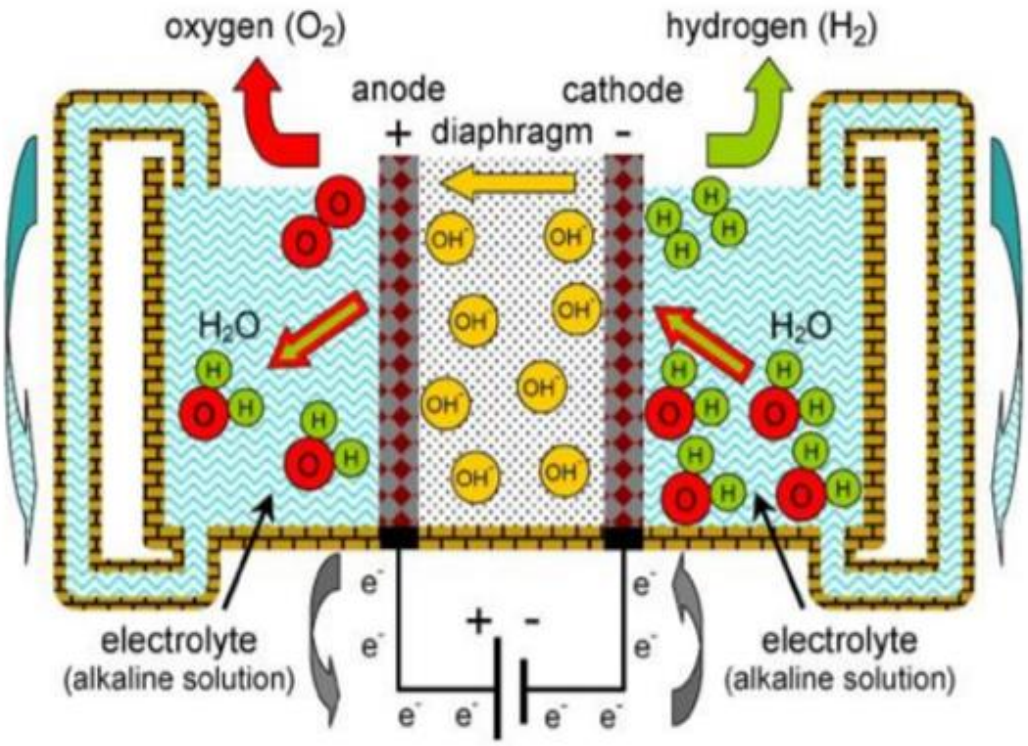

Fig. 2-9. Electrolyzer with anion exchange membrane [55].

The main reactions at the anode and cathode are based on Eq. 2-15 and Eq. 2-16, respectively.

$$2OH^- \rightarrow \frac{1}{2}O_2 + H_2O + e^- \qquad \text{Eq. 2-15}$$

$$H_2O + e^- \rightarrow \frac{1}{2}H_2 + OH^- \qquad \text{Eq. 2-16}$$

The overall reaction of the electrolyzer with the anion exchange membrane is in equation 2-17.

$$H_2O \rightarrow H_2 + \frac{1}{2}O_2 \quad \Delta H = 288\text{kJmol}^{-1} \qquad \text{Eq. 2-17}$$

Hydroxide ions (OH^-) are produced during the hydrogen evolution reaction (HER) and are transferred to the anode across the membrane in the moderate alkaline environment of the AEM electrolyzer. The OH^- exchanged is an anion that names the AEM in the same way as the proton (H^+) is the charge carrier in the acidic PEM system.

Platinum group metals (PGM) as catalysts and costly titanium bipolar plates are necessary for PEM electrolyzers to survive the extremely corrosive acidic surroundings, but non-PGM catalysts and steel bipolar flats are adequate to produce the AEM hydrogen efficiently.

In an AEM electrolyzer, the diluted KOH solution is safer to handle than an alkaline electrolyzer with a pH of 14.

When OH^- is returned to the anode of an electrolyzer, it is consumed in the oxygen evolution reaction (OER). This way, the OH^- content in the electrolyte is maintained by the electrode reactions alone and only water is needed to be added.

The OER is triggered by the voltage differential at the catalyst surface of the anode and the oxygen produced is removed by the gas diffusion layer and by the electrolyte circulation.

Enapter's modular electrolyzers can generate 500 NL per hour of green water, at a purity of 99.9% at 35 Bar using 0.4 L of water and 2.4 kWh of renewable energy, using AEM water electrolysis [72].

2.3 Electrocatalysis in water electrolysis

An electrocatalyst is a substance that reduces the activation energy of the electrode reaction of interest and increases the efficiency of the electrochemical device. The activity of the catalyst depends on its intrinsic properties and surface area. The activity of electrocatalysts is commonly taken as the activation overpotential at a certain reaction rate (current), or the values of the exchange current density and the Tafel slope. Activation overpotential is created due to the resistance of the reaction at the surface between the electrode and the electrolyte. Activation overpotential, if there is no mass transfer limitation or ohmic losses, is expressed by the relationship between current density (i) and activation overpotential (η_{act}) by the Tafel equation in Eq 2-18 (valid only at high overpotentials).

$$\log|i| = \log|i_0| \pm \frac{\alpha nF}{2.3RT}\eta_{act} \qquad \text{Eq. 2-18}$$

In the Tafel equation (2-18), α is the transfer coefficient, and i_0 is the exchange current density. The Tafel equation is used to calculate the Tafel slope and exchange current density to compare the activity of the electrocatalyst. Catalysts with a high exchange current density and low Tafel slope are desirable. If the electrocatalyst has a larger surface area, less current is applied to each unit of area, and hence the activation overpotential naturally decreases. Hence, a good catalyst should ideally have a high intrinsic activity and a high active surface area. In general, the electrocatalyst should have high catalytic activity, be corrosion resistant, and have high electrical conductivity.

The hydrogen evolution reaction (HER) is one of the most studied electrochemical reactions. Although electrodes with good performance are now available, reducing the potentials as much

as possible and thus reducing the energy consumption of the electrolysis process is still one of the interesting topics. Bo Chris was the first scientist to study the kinetics of the hydrogen evolution reaction and its kinetics on various metals. He investigated the effects of copper, gold, molybdenum, palladium, ruthenium, and iron on the reaction of hydrogen evolution in acidic and alkaline environments and calculated their electrochemical parameters. He showed the calculated values for the exchange current density and the transfer coefficient as a function of metal and concentration [32].

In another study, Bockris evaluated and compared the bond energy between a metal and an adsorbed hydrogen atom. The results of this evaluation showed that the noble metals of the platinum group have the most optimal bond energy among other metals. They are followed by nickel metals, and finally, molybdenum and tungsten are the metals that have the highest bond energy with atomic hydrogen [33].

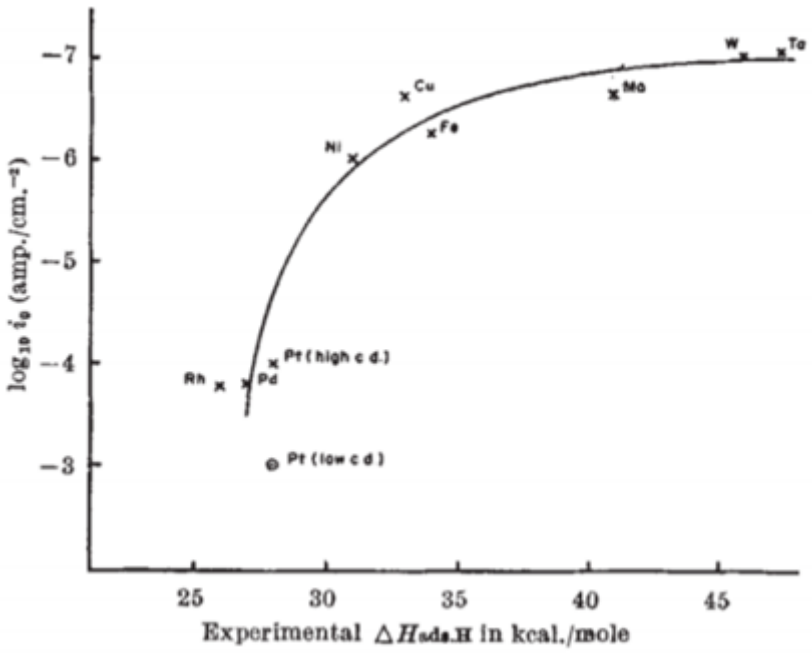

Fig. 2-10. Diagram of the dependence of the exchange current density on the bond energy of the metal and atomic hydrogen [33].

As a result, it can be said that the type of substance has a great effect on the kinetics of the hydrogen evolution reaction.

The mechanism of the hydrogen evolution reaction in an alkaline medium involves three steps and is shown schematically in Fig. 2-10. This reaction (Equations 2-19, 2-20, and 2-21) is either a combination of the Volmer-Tafel or Volmer-Heyrovsky-steps.

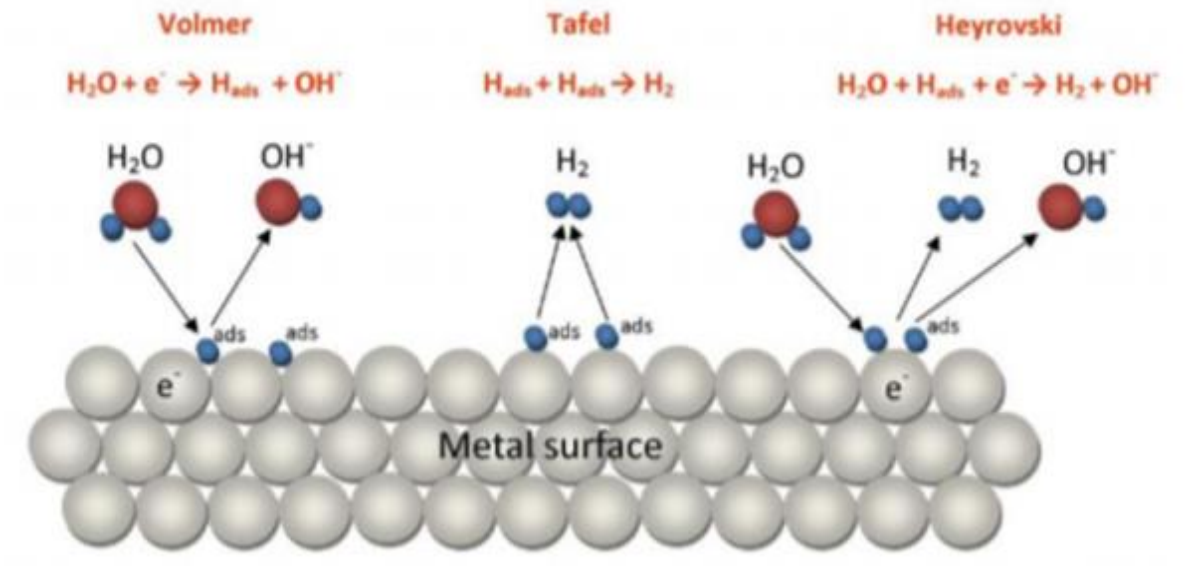

Figure 2-11. Schematic of the hydrogen evolution reaction in alkaline medium [56].

$M + H_2O \rightleftarrows M \ldots H_{ads} + OH^-$ Eq. 2-19

$M \ldots H_{ads} + H_2O + e^- \rightleftarrows M + OH^- + H_2$ Eq. 2-20

$2M \ldots H_{ads} \rightleftarrows 2M + H_2$ Eq. 2-21

The ability to absorb hydrogen depends on the inherent properties of the surface and its ability to bond with hydrogen. The activation energy of the hydrogen evolution reaction decreases with increasing adsorption energy. This means increasing the H_{ads} on the electrode. Therefore, if the H-M bond energy is too strong, the H_{ads} binds too strongly to the active sites at the surface and slows the second reaction step, Tafel, and lowers the overall reaction rate. Also, a weak H-M bond energy will slow down the adsorption step and also provide a low overall reaction rate. Therefore, the best hydrogen electrode should have moderate M-H bonding energy. The Volcano diagram in Figure 6-65 shows that the best and most active metal in hydrogen evolution reaction is platinum, situated near the peak of the volcano.

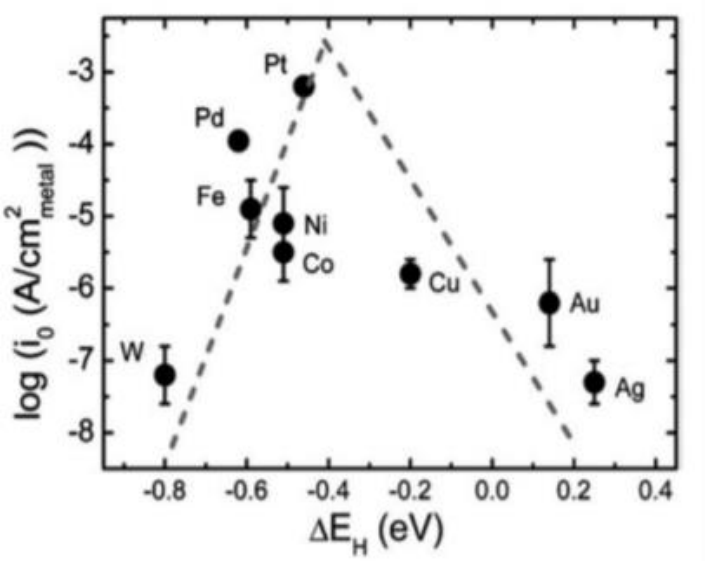

Figure 2-12. Volcano diagram illustrating the dependency of the electrocatalyst on metal and hydrogen strength in the hydrogen evolution reaction [57].

According to the diagrams and the results of various experiments, the best metals that can be used as a substrate are platinum group metals. But these metals have little abundance in nature. As a result, they will have a high price. Therefore, using them on a large scale will increase production costs. Finding cheap and abundant materials in nature with proper activity as a substrate in the hydrogen evolution reaction is one of the topics that has attracted the attention of researchers. Steel, nickel, copper, graphite, iron, titanium, and palladium-titanium alloy are among the materials that have been most commonly used as catalyst substrates [29]. In addition to the type of metal, physical properties such as size, type, and crystal structure are also effective in the electrocatalytic activity of the samples. Also, controlling the orientation of the metal catalyst surface or the crystal structure is effective in improving their activity because the activation energy to adsorb the reactants on the metal surface is a function of the distance between the adjacent atoms of the metal surface. Ahn et al. fabricated nickel metal with different physical properties such as dendrites, thin films, and nickel-based sheets by electrochemical coating on the carbon glass surface and compared their activity in the hydrogen evolution reaction. The results showed that the increase in electrocatalytic activity of the samples is directly related to the increase in the active surface area, so nickel dendrites have the most active and stable activity in the hydrogen evolution reaction [34].

In another study to increase the stability of the water electrolysis reaction in an alkaline environment, nickel hydroxide nanoclusters were layered on nine different substrates of intermediate metals, including copper, silver, gold, ruthenium, iridium, platinum, nickel,

vanadium, and titanium. The results showed that by layering nickel hydroxide on these metals, the overvoltage is significantly reduced [35].

The oxidation of water, also known as the OER, is a series of proton/electron-coupled processes that produce molecular oxygen. Two water molecules are oxidized in acidic conditions, leading to four protons (H^+) and one oxygen molecule, with a net transfer of four electrons. In acidic conditions, the most advanced OER electrocatalysts are iridium dioxide (IrO_2) and ruthenium dioxide (RuO_2) due to their high catalytic activity, leading to a low overpotential. IrO_2 is the industrial catalyst standard due to its superior longevity in comparison to ruthenium oxide. Under alkaline conditions, hydroxyl groups are primarily oxidized, leading to the formation of H_2O and O_2 through a process involving the same number of electrons. Noble metal oxides are still very good catalysts for the OER in alkaline electrolytes, but due to the alkaline environment, alternative and cheaper materials can be used. Much research has been done on the use of a single metal or alloy to catalyze the OER. Although there is no specific basis for the separation of cathode electrocatalysts, depending on the presence of different elements in each alloy, the non-noble metal catalysts can be classified into three groups [58]:

1. Nickel-based electrocatalysts
2. Iron-based electrocatalysts
3. Cobalt-based electrocatalysts

In the early part of the last century, it was found that Ni and its oxides have electrocatalytic activity toward OER in alkaline solution. In general, nickel, nickel alloys, and their composites are good catalysts for the oxygen evolution reaction. In addition to good activity, nickel also has high corrosion resistance in alkaline environments. Cobalt and iron, like nickel, are widely used as catalyst materials in alkaline water electrolysis systems due to their high stability, good performance, and low cost [36].

The production of nickel alloy in combination with other metals also improves its electrocatalytic properties. It is well known now that the addition of Fe to Ni improves the catalytic performance of Ni towards the OER significantly [74] Many researchers have synthesized different NiFe mixed compounds in an effort to create more effective OER electrocatalysts. Furthermore, electrochemical measurements have shown that the alloying of nickel and cobalt reduces the overpotential at a given current density [78]. In one study, a nickel-cobalt catalyst was deposited on a copper plate by electrochemical coating. The results

showed that by adding more cobalt to nickel in the alloy, the overvoltage of the water splitting will be reduced [37].

Stainless steel, typically an alloy of nickel, iron, and chromium [59-62], has recently gained renewed attention as the anode in alkaline water electrolysis. More sophisticated NiFe-based OER electrocatalysts with increased catalytic activity for efficient and long-lasting water electrolysis have recently been designed by researchers in response to the increasing demand for clean and renewable energy [75].

2.4 Synthesis of nanoparticle electrocatalysts

2.4.1 Nanomaterials

Nanotechnology is a field of engineering and technology that studies materials that are at least 1 to 100 nanometers in size in one dimension. Nanotechnology is the understanding and application of new properties of materials and systems in nano-dimensions that show new physical and chemical effects, mainly due to the dominance of quantum properties over classical properties. Nanomaterials are typically materials that are smaller than 100 nanometers in at least one dimension. Nano-sized materials have certain physical, chemical, and biological properties that cannot be found in larger sizes. Particle size is very important in nanotechnology because at the nanoscale, the dimensions of the material are very influential in its properties. The use of nanotechnology in the last century is one of the important fields of modern research. In nanotechnology, particles are about 1 to 100 nanometers in size, at which all the physical, chemical, and biological properties of chemical compounds are different. The improved properties of nanomaterials depend on their size, morphology, and distribution. These properties have created a new perspective in research. Because of this, new applications of nanomaterials are expanding rapidly. Applications of nanotechnology in fields such as medicine, cosmetics, food and nutrition, gene and drug transfer, environment, medicine, mechanics, chemical industry, electronics, space industry, energy science, etc. are expanding [17].

With the growth of industries, the use of more effective catalysts in the chemical and environmental industries to reduce environmental pollution and production costs has become increasingly important. Nanocatalysis is a combination of two growing areas of catalysis and new nanotechnology. Catalysts were among the first applications of nanotechnology on an

industrial scale. The use of fine particles in heterogeneous catalysis reduces the volume of the catalyst and allows the optimal use of the active component.

Various methods have been designed for the synthesis of nanomaterials. The choice of the optimal method depends on various factors, the most important of which are the desired properties of the product. After determining the characteristics of the product, according to the ability of the method to control the size, shape, distribution, and degree of agglomeration, cost, and amount of production, a suitable method for nanoparticle synthesis will be selected. The main difference between nanotechnology and conventional technologies is that in nanotechnology, "bottom-up" methods are preferred, while in conventional technologies, "top-down" methods are generally used.

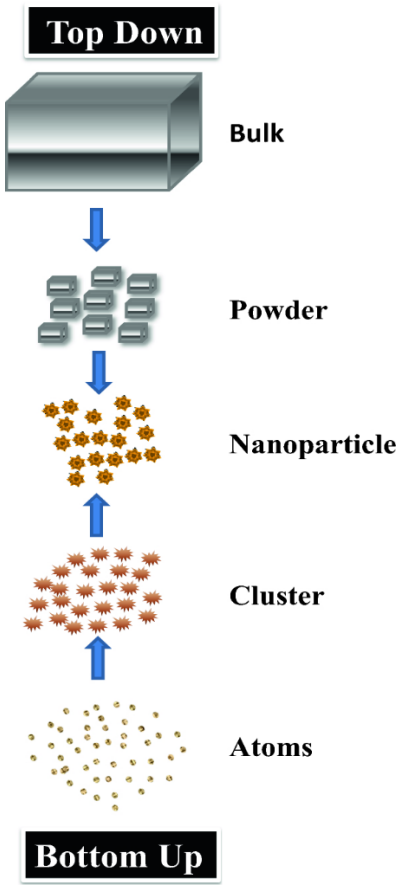

Fig. 2-13. Top-down and bottom-up approaches for nanoparticle synthesis [63].

The main difference between nanotechnology and conventional technologies is that in nanotechnology, "bottom-up" methods are preferred, while in conventional technologies, "top-down" methods are generally used. Fig. 2-13 shows a top-down and bottom-up approach for nanoparticle synthesis.

2.4.2 Bottom-up techniques

In bottom-up methods, the product is made of simpler materials, such as building an engine from its parts. In fact, what is done in this method is to put together atoms and molecules (which are smaller than the nanoscale) to make a nanometer-sized product. Bottom-up methods usually do not have lesions, although this is not necessarily the case. For example, part of a self-assembly system may require the help of a "component" for the self-assembly process that is not present in the final product and is therefore removed from the system. Figure 2-13 shows the fabrication of nanoparticles from atoms or molecules. Although many products can be produced using these processes, the variety of possible structures with this production method is limited. In order to achieve regular structures, bottom-up processes must be complemented by the self-assembly of individual particles.

One of the bottom-up synthesis methods is the chemical reduction method, which is used to make metallic nanoparticles. In this method, there are three basic components, which are: metal precursor, reducing agent, and stabilizing agent. By selecting each of these three factors and controlling the synthesis conditions, the shape, composition, and size of metal nanoparticles can be controlled.

2.4.3 Chemical reduction processes

The synthesis of metal nanoparticles by the metal salt reduction method is one of the most common methods that has been widely reported. In this method, metal ions are reduced by organic or inorganic reducing agents in the presence of various stabilizers and converted into metal nanoparticles. The first standard and reproducible instruction for the synthesis of metal colloids was the chemical reduction reaction of gold salt with sodium citrate, published by Turkevich in 1985 [73]. He also explained the mechanism of nucleation, growth, and accumulation in this reaction, the basis of which is still valid.

In chemical reduction, a metal precursor is first dissolved in a suitable solvent. Due to the dissolution of the metal precursor, the metal cations are dispersed in the solvent medium. A reducing agent is then added to the solvent and, by providing electrons, regenerates the metal cations and neutralizes them. An example of a selective reducing agent is sodium borohydride. In the presence of epoxides, esters, lactones, acids, nitriles, or nitro groups, sodium borohydride solutions in ethanol catalyze the reduction of aldehydes and ketones. $NaBH_4$ is similar to

$LiAlH_4$ but has lower reactivity. Only aldehydes, ketones, and acid chlorides can be reduced to alcohols; esters, amides, acids, and nitriles are left largely unaffected. In the presence of halides and epoxides, it can act as a nucleophile. As a result, by adding a reducing agent, metal cations can be neutralized, and nucleation and growth can occur. As nucleation and growth occur, nanoparticles become larger, and if left unchecked, the growth progresses to such an extent that the particle size exceeds 100 nanometers. Stabilizers are used to prevent this. These stabilizing agents, which are usually polymers, prevent nanoparticles from growing by being placed around them and determine how much the nanoparticles grow [2].

In this process, as a method of producing nanoparticles from the bottom up, the production of large particles can be prevented. This process is divided into two forms of reduction in the aqueous phase and reduction in the organic phase. Factors affecting the production of metal nanoparticles in this way are:

1. Metal composition: such as metal salts and metal complexes

2. Solvents: such as water, polar organic solvents, and non-polar organic solvents

3. Reducing agents: such as hydrogen gas, hydrazine, hydride compounds, organic reducers such as alcohols and metals

Many first-order intermediate metals such as Au^{3+}, Ag^{+}, Cu^{2+}, Ni^{2+}, Co^{2+}, Fe^{3+}, $Fe^{2+,}$ and many second- and third-row elements of the periodic table are reduced with the above reducing agents. In some cases, organic coatings, which are commonly used to prevent particles from sticking together in aqueous media, are also used as reducing agents. In this regard, one of the known reactions is the Turkovich method, which has been used to make gold nanoparticles [14]. In this method, a gold colloid is prepared by adding sodium nitrate as a reducing and stabilizing agent to dilute and boil the $HAuCl_4$ solution [14].

4. Stabilizers (including stabilizing agents, ligands, preservatives, and foaming agents) and their mechanisms of action (including preventing uncontrolled particle growth, preventing particle agglomeration, growth rate control, particle size control, and solubility of particles in different solvents)

One of the factors used by chemical reduction reactions to control the growth phase of particles is the use of various stabilizers. Stabilizers can limit the growth and aggregation of particles, and thus the growth process that occurs through the successive accumulation of primary nuclei,

eventually leading to the production of larger particles. Eventually, the size of the metal particles is reduced to the nanometer range.

In this process, nanoparticles are stabilized in two ways to prevent agglomeration:

1. Electrostatic stability: The adsorption of ions on the surface, which produces a double layer of electricity and causes a repulsive force between particles.

2. Spatial stability: The metal core is surrounded by materials that are bulky, including polymers, surfactants, and other bulky materials.

Important parameters that can be controlled in this method are:

I) The average size is affected by the concentration of the reducing agent, stirring speed, and temperature.

II) The size distribution depends on the rate of addition of the reducing agent and the rate of stirring.

III) Particle stability is affected by the composition of the solution.

2.4.4 Annealing process

The main chemical method for making nanoparticles is the process by which an environmentally soluble substance is transformed into an insoluble structure. The principles of this synthesis method are repeated in many other methods of synthesis from the solution phase. In general, the formation of low-soluble products from the aqueous phase is the basis of this method. The process of chemical fouling involves the stages of nucleation and growth. It is these two steps that lead to the production of quality products. Many of the compounds formed by this method (especially at low temperatures) are amorphous. Therefore, to obtain products with a suitable crystal structure, it is necessary to perform secondary thermal processes such as annealing or calcination.

In the synthesis procedure of nanoparticles, the heat treatment process changes the physical and sometimes chemical characteristics of the material so that its flexibility and stiffness are increased. It entails the heating of material above its temperature, the preservation of an acceptable temperature for an adequate time, and subsequently cooling.

Atoms move into crystal gills during annealing, decreasing the number of dislocations and resulting in changes in ductility. It recrystallizes as the substance cools.

The size and the phase composition of a crystal grain that eventually characterize the qualities of the material rely on the heating pace and cooling rate of various alloys, including carbon steel. After the rinsing process, cold and hot work modify the structure of the metal, so additional heat treatments may be employed to acquire the necessary features. Heat treatment can be used to adjust from significantly hard to softer and more ductile with consideration of the chemistry and the phase structure.

High-performance nanocomposites in the next generation are vital to the achievement of ultrasmall size ferromagnetic characteristics. During the annulment process, however, nanoparticles are generally developed and agglomerated, destroying small dispersion.

2.5 Characterization Techniques

2.5.1 Scanning electron microscopy (SEM)

The scanning electron microscope is one of the most popular types of electron microscopes and has found many applications, especially in nanotechnology. SEM (scanning electron microscope) which is one of the electron microscopes, is one of the most popular microscopic methods that, in addition to producing magnified images, can be used for chemical analysis and other studies if equipped with additional equipment. The basis of this microscope is the interaction of the electron beam with the matter. The rays emitted from this interaction can be used for investigations. The principles of SEM performance are based on three principles that are linked in a chain:

1. Interaction of electron beam with sample.

2. The possibility of producing and controlling the electron beam characteristics of the scanner in electric and magnetic fields.

3. The possibility of detecting the rays emitted by the sample due to its interaction with the input electron beam.

When a scanning electron beam strikes a sample, it interacts between them. The result is the emission of rays that are detected with the help of detectors and reveal the properties of the

material. Fig. 2-14 shows a schematic of the beams emitted from the sample. The type of information obtained in this way depends on the interaction of the beam with the sample.

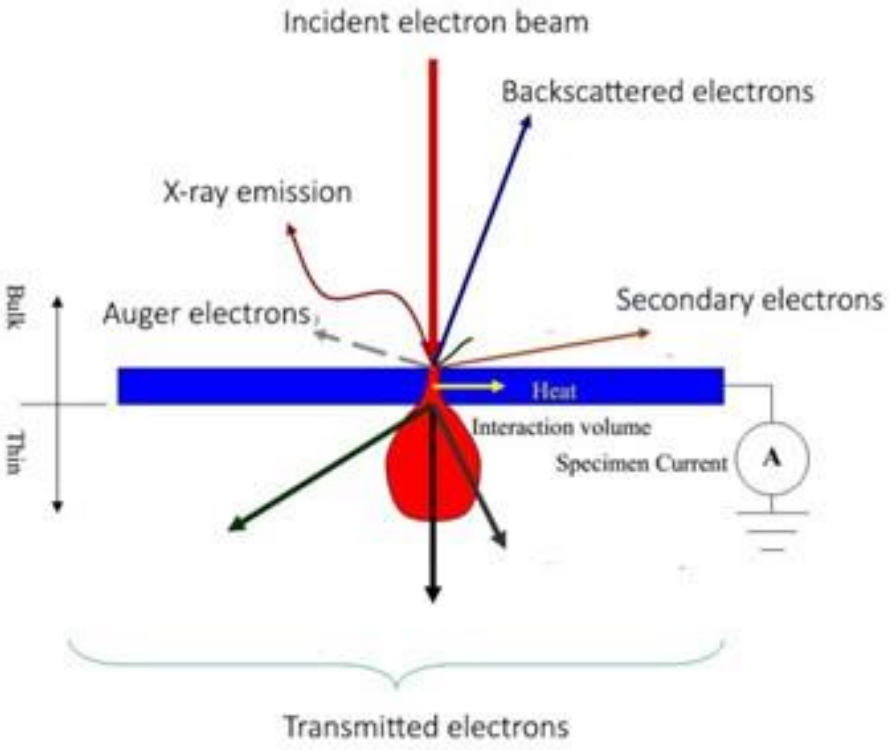

Fig. 2-14. Interaction of electron beam with sample [96]

Electron beams entering the sample typically contain electrons with energies of 1 to 12 electron volts that behave very differently when they encounter matter, including:

1. The electron may be ineffective and pass through the sample.

2. The electron may scatter elastically, changing direction without changing its energy.

3. The electron may scatter and refract, scattering in a preferred direction determined by the crystal structure of the sample.

4. Electrons can be inelastically scattered and change in energy and direction.

5. The electron may be absorbed by the material substrate.

2.5.2 Energy-Dispersive X-ray spectroscopy (EDX)

X-ray energy diffraction spectroscopy is a method used to analyze the structural or chemical properties of a sample. This method relies on examining the interaction between an X-ray

excitation source and a sample. The descriptive capabilities of this method are generally based on the general principle that each element has a unique atomic structure that enables a unique set of peaks in its X-ray spectrum. To stimulate the emission of a characteristic X-ray from a sample, a high-energy beam of charged particles such as an electron or proton, or an X-ray beam, is focused on the sample being studied. An atom inside a resting sample contains base electrons at discrete energy levels or electron layers attached to the nucleus. The applied beam may excite an electron in the inner shell and drive it out of the shell, creating an electron hole in the electron's anterior position. An electron with less than one outer layer then fills the hole, and the energy difference between the high-energy and low-energy layers can be released in the form of an X-ray. The number and energy of X-rays emitted from a sample can be measured using an energy diffraction spectrometer. Since the energy of X-rays represents the energy difference between the two layers as well as the atomic structure of the element from which they are emitted, it is possible to measure the composition of the sample elements, as shown in Fig. 2-15.

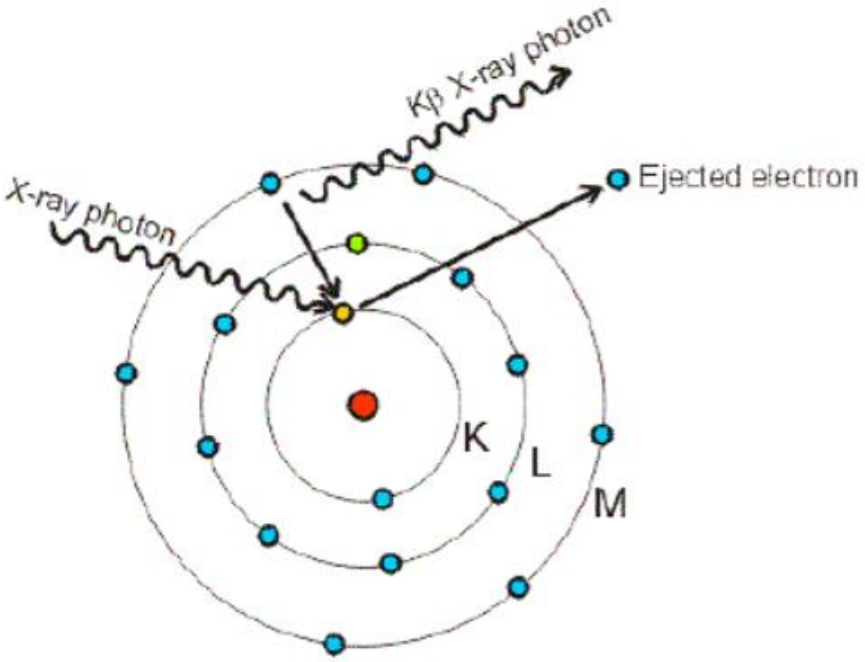

Fig. 2-15. Atomic structure changes as a result of EDX [98].

Eq. 2-24, presented by Moseley for the relationship between the characteristic X-ray wavelength emitted from the atom and the atomic number, as well as Eq. 2-25, shows that the energy levels in the electron layers have different values according to the atomic number. Energy levels are a unique value for each element.

$E = hv = hc/\lambda$ Eq. 2-24

$z = \lambda - 1/2$ Eq. 2-25

Therefore, by measuring the energy or wavelength characteristic of electrons transferred from a higher layer to a lower layer, we can identify the element associated with it. EDX is a more efficient method for elements with a larger atomic number because the radiation emitted from light elements has a low energy (less than 0.7 kV). Because quantitative analysis of quantitative analysis results requires higher-energy X-rays, there is an error in using EDX to determine elements with a small atomic number [96].

2.5.3 X-ray powder diffraction (XRD)

X-ray diffraction is an old and widely used technique in studying the properties of crystals. In this method, X-ray diffraction by the sample is used to investigate the characteristics of the sample. XRD can be used to determine the general quantities of crystal structure such as lattice constant, lattice geometry, qualitative determination of unknown materials, crystal phase determination, crystal size, single crystal orientation, stress, stress, lattice defects, etc. It is observed that in X-ray diffraction by the crystal, the intensity of the X-rays reflected from the crystal, which are scattered elastically at each atom, will be maximal at certain angles without changing the wavelength. The X-ray collision with an atom or molecule causes the electrons of the atom or molecule to oscillate and oscillate.

If the frequency of the reflected light is the same as the initial light frequency, this phenomenon is called Rayleigh scattering. From a quantum point of view, electromagnetic waves are composed of photons. The associated photon energy of an electromagnetic wave depends on the frequency according to Eq. 2-26.

$E = hv$ Eq. 2-26

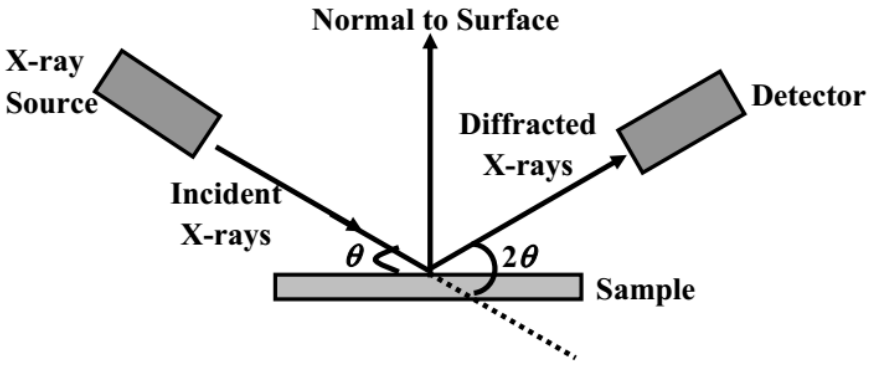

Fig. 2-16. Principle of XRD analysis [64]

Since the frequency of light does not change in Rayleigh scattering, according to Eq. 2-26, the energy of single photons does not change either. The basis of XRD is Rayleigh's scattering of crystal plates. Quantities obtained from the diffraction of a crystal include the maximum peak angle, the relative maximum intensity, and the width of each peak. These parameters form the basis of XRD. There are many uses for XRD. As shown in Fig. 2-16, the X-ray strikes and reflects off the crystal plates. Incident rays from the upper surface and diffracted rays reflected from the lower surface have path differences. This path difference depends on the angle of radiation and the distance between the two plates and is determined by Eq. 2-27.

$$\Delta x = 2d\sin(\theta) \qquad \text{Eq. 2-27}$$

Δx is the difference in the path, d is the distance between two planes, and θ is the angle between the ray and the plane. This leads to a phase difference between the two rays, which is determined by Equation 2-28.

$$\Delta\emptyset = \frac{2\pi}{\lambda}\Delta x \qquad \text{Eq. 2-28}$$

ΔΦ is the phase difference, λ is the wavelength of the ray, and Δx is the path difference between the two rays. If this phase difference is an integer multiple of π, the two rays converge constructively. Each optical device receives incident and diffracted rays, despite the distance between them, as a whole or, to put it better, as an average. This co-phase shrinkage corresponds exactly to the maximum intensity of the X-rays emitted, which is displayed as a peak in the XRD pattern. This pattern is repeated over the entire length of the two plates. This pattern is also repeated between the lower plates. This can be summarized as Eq. 2-29.

$$n\lambda = 2d\sin(\theta) \qquad \text{Eq. 2-29}$$

Equation 2-29 is Bragg's law. Multiple plates can be considered for each crystal. These plates vary in their spacing between plates. Bragg conditions for each plane occur at a certain angle, assuming the X-ray wavelength is constant. In crystallography, plates are identified with Miller indices [97].

2.5.4 Brunauer-Emmet-Teller (BET)

BET theory is about the adsorption of solids. One of the important applications of this theory is to explain the behavior of gas molecules in the adsorption phenomenon on solid surfaces. This method is also used to calculate the specific surface area of adsorbents. The theory is named after three scientists, Stephen Brunauer, Paul Hugh Emmett, and Edward Teller, who proposed the theory in 1938.

The BET analysis method is used to measure the specific area and density of material nanotubes. The principles of working with this device are based on measuring the absorption of neutral gases such as nitrogen at a constant temperature at the surface of nanotubes.

Because measuring the specific area for nano aerosols is difficult and problematic, the BET method has now replaced the TEM method.

The Langmuir isotherm is usually expressed in terms of the adsorption of a single layer of gas molecules on a solid surface with a medium gas pressure at a constant temperature. The fraction of the coated adsorbent surface, θ, is defined by Eq. 2-30.

$\alpha P/1+ \alpha P = \theta$ Eq. 2-30

α is a constant value, and P is the gas pressure.

Generally, in the adsorption process, atoms or gas molecules will be adsorbed on a solid surface. The amount of gas adsorbed on the solid surface depends on the amount of contact surface, temperature, gas pressure, and the strength of the gas-solid interaction. In the BET technique, nitrogen is commonly used because of its cheapness, availability, high purity, and strong interaction with most solids. Also, due to the weak interaction between gases and solid phases, the solid surface cools to absorb a significant amount of nitrogen on the solid surface. A constant amount of nitrogen gas enters the sample cell in stages. This nitrogen gas has a pressure less than atmospheric, for which a relative vacuum must be created. After saturation pressure and reaching the saturation position where all active positions are occupied, no further

adsorption occurs. During the adsorption process, the detectors will measure the changes in gas pressure.

Once the adsorbed layers have formed, the sample will be removed from the nitrogen atmosphere. By heating the solid phase, the adsorbed nitrogen gas will be expelled from its surface. This amount of gas will be measured. Finally, the amount of adsorbed nitrogen gas will be plotted as a function of relative pressure. The BET diagram is shown in Fig. 2-17, where *I* is the width of the origin of the diagram and *A* is the slope of the diagram.

The BET theory diagram is an extended form of Langmuir theory based on the Langmuir hypotheses, which are:

1. The surface of a solid is homogeneous, which means it is composed of one type of substance, and there are a certain number of places for adsorption on the surface.
2. Each area does not absorb more than one molecule, in which case a single layer of molecules will be adsorbed on the surface of the solid.
3. The adsorbed gas molecules in the vapor phase have ideal behavior, i.e., there is no interaction between the gas molecules and the adsorbent surface.
4. The adsorption process is considered an equilibrium process similar to the condensation and excretion of gas molecules on the surface of a solid.

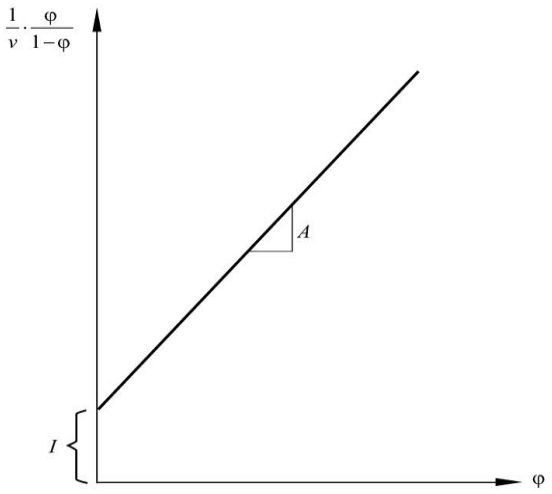

Fig. 2-17. BET diagram [65]

Eq. 2-31 is based on Langmuir's assumptions.

$$\frac{1}{v[(P_0/P)-1]} = \frac{c-1}{v_m c}\left(\frac{P}{P_0}\right) + \frac{1}{v_m c} \qquad \text{Eq. 2-31}$$

Where v_{mc} is the volume of gas required to form a monolayer, v is the total volume of adsorbed gas, and P and P_0 are the pressure tested and saturated pressure, respectively. C is a constant value that depends on the enthalpy of adsorption of the adsorbed gas on the powder sample.

Also, the value of parameter c is calculated by Eq. 2-32.

$$c = exp\left(\frac{E_1 - E_L}{RT}\right) \qquad \text{Eq. 2-32}$$

Where E_1 is the enthalpy of adsorption for monolayer formation and E_L is the enthalpy of adsorption for the formation of liquid on the surface.

2.5.5 Barrett-Joyner-Halenda (BJH)

The BJH method is used to identify particle microstructures. In this test, which uses nitrogen uptake and excretion on particles, the diameter and specific surface area of the particles are calculated. Also, pore volume and size distribution are calculated by the BJH method. In this method, certain intervals are considered for the size of the holes. At these distances, based on the theories of monolayer or multilayer adsorption, the amount of surface in contact with nitrogen as well as the volume of nitrogen adsorbed are calculated. Therefore, apart from calculating the surface area and volume of cavities, at certain distances from the size of the cavities, the amount of change in the volume of adsorbed gas relative to the size of the cavities is obtained. By drawing this parameter according to the size of the holes, its distribution is also calculated. The maximum value of this graph is declared as the average hole size calculated by the BJH method. The shape of the diagram shows how the size of the holes is distributed in the sample [25,24]. While BJH is a distribution size estimation method, the BET measures the specific surface of the materials. In BET, v is a volume that is normally less than the largest P/P0, where, like in BJH, V is a certain volume that indicates a volume with a variety of pore sizes.

2.6 Electrochemical measurements

The working electrode, counter electrode, and reference electrode comprise the three-electrode system. The role of the reference electrode is to serve as a reference while measuring and adjusting the potential of the working electrode. The reference electrode should be based on a fast and reversible electrochemical reaction to obtain a stable reference potential. It should not

pass any current and be placed close to the working electrode to minimize uncompensated electrolyte resistance. In addition to a reversible hydrogen electrode (RHE), the Hg/HgO electrode and the Ag/AgCl electrode are the most frequent laboratory reference electrodes. In a three-electrode design, the counter electrode's sole function is to pass all the necessary current to balance the current recorded at the working electrode. The counter electrode should ideally have a large surface area and involve reactions that do not impact the working electrode performance.

2.6.1 Linear Sweep Voltammetry (LSV)

LSV is known as a voltammetric technique, in which the current value is observed while the potential is swept linearly with time from an initial (starting) potential, typically where no reaction occurs, to a final potential well into the potential region where you expect a reaction to happen. This method can give many characteristic features where oxidation and reduction processes are observed in the current response as positive or negative current contributions, respectively.

The scan rate of the potential ramp of the working electrode is very important and should be as low as possible when the ambition is to measure catalyst activity by means of approximated steady state currents (quasi-steady state).

2.6.2 Cyclic Voltammetry (CV)

Cyclic voltammetry is one of the best ways to investigate the mechanism of reactions based on a potential sweep. Because of these capabilities, cyclic voltammetry is almost always used as a useful method for systems being studied for the first time.

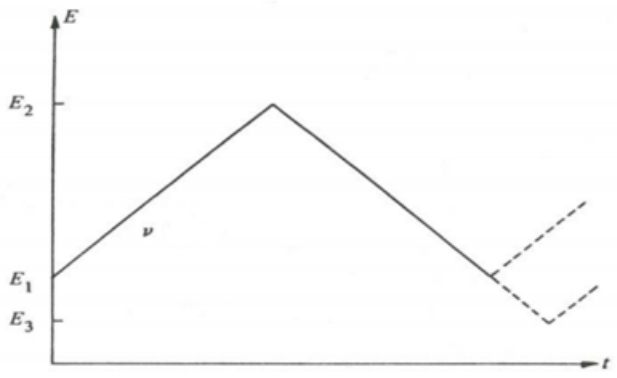

Fig. 2-18. Potential-time profiles for cyclic voltammetry [55].

In the cyclic voltammetry method, the potential is scanned from the initial value of E1 (initial) to E2 and then inverted to the value of E1 or E3 as shown in Fig. 2-18. E2 is often called the higher reversal potential, while E1 (or E3) would be the lower reversal potential. Fig. 2-19 shows a selection of voltammograms of a nickel electrode in an alkaline electrolyte [50]. It is clear that the nickel surface changes depending on the potential and cycle history. The blue curve represents the first cycle, where there is an oxidation current observed at 0.30 V corresponding to α-$Ni(OH)_2$ formation. A further increase in potential leads to another oxidation peak at about 1.30 V, where β-NiOOH is formed. This species is subsequently reduced in the negative-going sweep at slightly more negative potentials. Interestingly, the β-NiOOH redox peak is observed in both cycles going to high potentials, while the α-$Ni(OH)_2$ is not. If the upper reversal potential is higher than about 0.50 V, the α-$Ni(OH)_2$ is not observed on subsequent cycles.

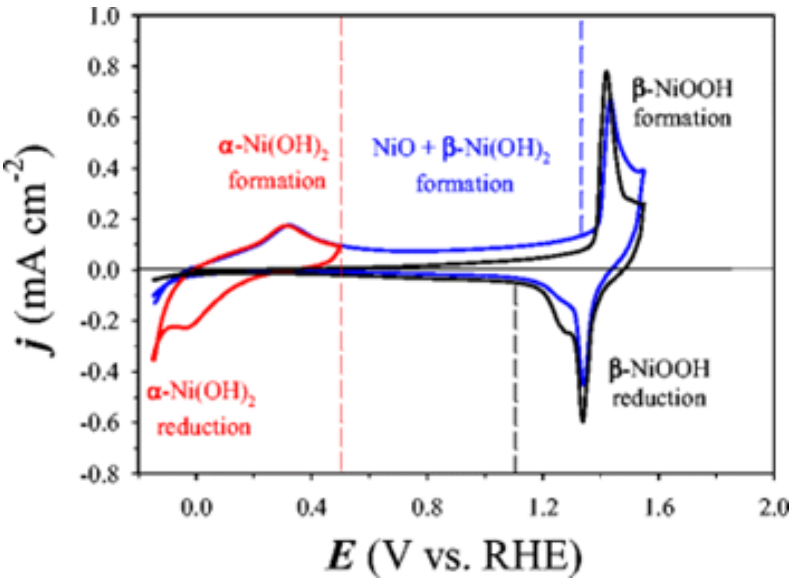

Figure 2-19. Cyclic voltammograms of a nickel electrode in alkaline electrolyte with 25-30 wt% (KOH)aq and a temperature of ambient to 120 °C [50].

As illustrated in figure 2-19, cyclic voltammetry is a powerful tool to investigate electrode reactions and reaction mechanisms, which often depend on the upper/lower reversal potential, scan rate, electrode material, electrolyte and other experimental conditions.

2.6.3 Electrochemical Impedance Spectroscopy (EIS)

EIS is one of the most powerful methods in electrochemistry due to the wide range of time constants that can be investigated. The EIS method can be used to measure electrode kinetics

in an electrochemical cell, from slow mass transport processes to fast electron transfer reactions.

Any solid or liquid can pass current when voltage is applied to it. If a constant voltage (dc) is applied to the sample, the applied voltage to the current ratio (V/I) is known as the resistance. And if the applied voltage to the sample is variable (ac), the V/I ratio is called the impedance. Impedance changes as a function of applied voltage changes. If the impedance measurement is done in a frequency range and the results are plotted on the appropriate axis, it is possible to relate the results to the physical and chemical properties of the material. This method is called electrochemical impedance spectroscopy [66].

Recently, the EIS method has been used to describe the process within a porous electrode and on complex surfaces [67].

An EIS is usually performed by applying an alternating current (AC) signal to an electrochemical system at steady-state and then measuring the current response. The AC perturbation is commonly small, making EIS essentially a non-destructive technique.

If a small sine voltage according to Eq. 2-33 is applied to an electrochemical system, a sine current response in the form of Eq. 2-34 will be observed. Due to the lack of rapid response of relaxation processes or the release of dipoles (rotation of dipole components in response to the applied alternating electric field), a phase change is obtained, which is given in Eq. 2-35.

$$U(t) = U_m \sin(\omega t + \varphi_u) \qquad \text{Eq. 2-33}$$

$$I(t) = I_m \sin(\omega t + \varphi_i) \qquad \text{Eq. 2-34}$$

$$\varphi = \varphi_u - \varphi_i \qquad \text{Eq. 2-35}$$

Where U_m is the voltage amplitude, I_m is the current amplitude, and φ is the phase separation between the voltage and current, which depends on the reactions that occur in the system [3].

At high frequencies charging currents will approach zero and only the uncompensated resistance can be measured. Therefore, the value of the extrapolated high-frequency intercept with the real axis in a complex impedance or Nyquist plot is commonly read off as the uncompensated resistance.

2.6.4 Constant-potential electrolysis - stability test

To measure stability, the chronoamperometric technique or constant-potential electrolysis is used as a stability test. Chronoamperometry is an ammetric technique in which a potential step is applied to the working electrode and the current is measured as a function of time and plotted as a graph of the electrode stability during the oxygen evolution reaction.

2.7 Electrochemical surface area (ECSA)

The active surface area of some catalyst materials is quite straightforward to measure. For example, by measuring the charge associated with the adsorption or desorption of one monolayer of underpotential-deposited hydrogen (UPD-H) in a CV of a platinum electrode, one can reliably determine the active surface area of the platinum catalysts. Assumptions and estimates must be made when attempting to estimate the active surface area of Ni materials due to the complexity of Ni electrochemistry, leading to inaccurate results. Especially for electrodes used for OER, where oxides are present at the surface. Despite the variety of ECSA methods available for Ni-based materials, there is no agreement on the most accurate and trustworthy method, implying that there are concerns with each method's application. A material's ECSA is affected by its form, synthesis, surface composition, and size. The Alpha, Oxalate, Capacitance, and Beta methods have recently been effectively examined and compared for Ni wire, Ni foams, and shape-specific spherical, urchin, and triangle Ni-NPs using electrochemical active surface area methodologies provided in the literature [68].

2.7.1 Faradaic and capacitive currents, from CV and EIS

Two types of processes occur at the electrodes. One of those processes is the transfer of charge at the interface between the electrode and the solution by oxidation and reduction reactions that follow Faraday's law, called faradaic processes. Sometimes, electrodes in which faradic processes occur are called charge transfer electrodes. Under unfavorable conditions, thermodynamically and kinetically, no charge transfer reaction takes place in a range of potentials. But processes such as adsorption and desorption can occur, and the structure of the solution electrode interface can be changed by changing the potential or composition of the solution. These processes are called "non-faradic processes". In non-faradic processes,

electrons are not exchanged. Both faradic and non-faradic processes occur in electrode reactions.

The distinction between Faradaic and non-Faradaic electrode processes is that the electrode charge, voltage, and composition go to constant values following the application of a constant current in a Faradaic process. Instead, the load is gradually stored in a non-Faradaic (capacitive) process.

To obtain comparable values [10], electrochemical parameters such as electric current or electrode reactions must be standardized. The loadings are typically employed for powder catalysts to quantify these values, but these are not readily available for flat film catalysts.

The planned surface area is often used as a reference for flat films. The challenge here is how the particular active surface area can be determined to measure the activities of various catalyst materials.

One technique frequently employed is to estimate the surface area using the electrochemical double layer capacitance.

An estimation of the double layer capacitance can be obtained using cyclic voltammetry in a potential region where there are no faradaic reactions [69]. The plot of the current at a specific potential should be linear versus scan rate, and the slope of this line gives the double layer capacitance. Subsequently, the electrochemical surface area can be obtained by dividing the double layer capacitance over the specific double layer capacitance of the electrode material. For nickel alloys, this is not easily obtainable, and therefore the double layer capacitance values can only be used as a qualitative indication of the electrochemical surface area.

A differential capacitance measurement (DCM) is utilized with varied scan speeds in a small potential range in an electrochemical double layer capacitance measurement. In the absence of the Faradaic reaction, this measurement matches the resultant differential capacitance with the double layer capacitance [11]. The capacitive double-layer charge is responsible for the measured current (i_C) in the chosen potential window. To calculate C_{dl}, plotting the slope of a curve with scan rate (v) is all that is needed to determine its value, according to Equation 2-36.

$$i_C = vC_{dl} \qquad \text{Equation 2-36}$$

Finally, to obtain the ECSA, the value of C_{dl} is divided by the specific capacitance (C_S) of the sample at the same electrolyte, using Equation 2-37.

$$ECSA = \frac{C_{dl}}{C_S} \qquad \text{Equation 2-37}$$

The roughness factor (RF) can also be calculated using the ECSA estimate. RF is calculated by dividing the real area by the geometric area.

Chapter 3

Experimental

3.1 Synthesis

To ensure the accuracy of the results, three replicates of each experiment were conducted with three samples of each catalyst.

3.1.1 Solution preparation

Two sets of solutions were prepared for the synthesis of OER catalysts, one containing metallic precursors and one containing a reducing agent. Each precursor solution contained 6.8 mmol $Ni(NO_3)_2 \cdot 6H_2O$ in addition to a second salt for bimetallic catalyst fabrication, $Co(NO_3)_2 \cdot H_2O$ for synthesis of Ni_xCo_y and $FeCl_3 \cdot 6H_2O$ for Ni_xFe_y. The precursors were dissolved in 60 ml of distilled water and the Co and Fe salts were adjusted to their respective ratios to the nickel ion in accordance with Table 1. The reducing solution comprised 0.1 molar potassium hydroxide and 13.6 mmol sodium borohydride. Both solutions were stirred at 750 rounds per minute.

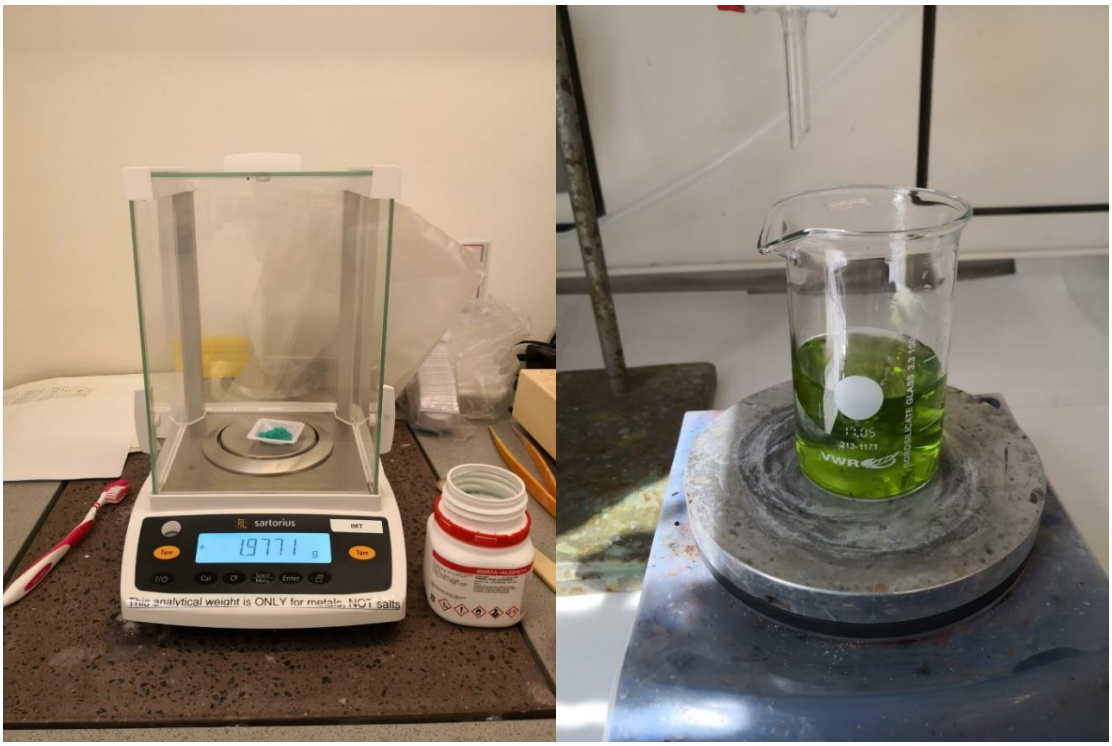

Fig. 3-1. Ni solution preparation.

There was no need to use more than 100 ml of the reducing solution for the Ni_3X_1 and Ni_1X_1, but 200 ml was needed for the Ni_1X_3.

Table 3-1. Nominal compositions of all catalysts synthesized in this work.

Sample Name	**Ni**	**Co**	**Fe**
Ni	1	-	-
Ni_3Co_1	3	1	-
Ni_1Co_1	1	1	-
Ni_1Co_3	1	3	-
Ni_3Fe_1	3	-	1
Ni_1Fe_1	1	-	1
Ni_1Fe_3	1	-	3

3.1.2 Reaction

Prior to mixing, the temperature of the precursor solution was adjusted by placing it in a tray filled with ice while also containing a magnetic stirrer that rotated at 750 rotations per minute (Figure 3-2a). This state was maintained for ten minutes. Subsequently, the reducing solution was introduced to the precursor solution in the form of droplets in a stepwise manner at a stirring speed of 900 rpm (Figure 3-2b). After adding all the reducing solution, the mixture was allowed to stand for a further 10 minutes while spinning at 750 rotations per minute so that the reaction could take place in its entirety. Representative solutions of NiFe and NiCo catalysts are shown in Figure 3-3.

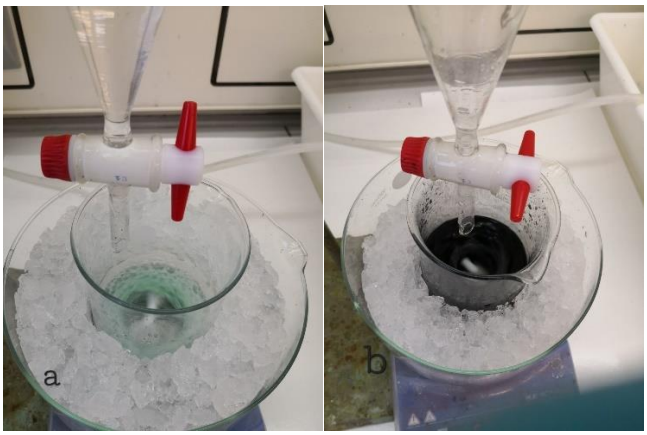

Figure 3-2. Pictures of the (a) precursor solution prior to mixing and (b) dropwise addition of reducing solution to the precursor solution.

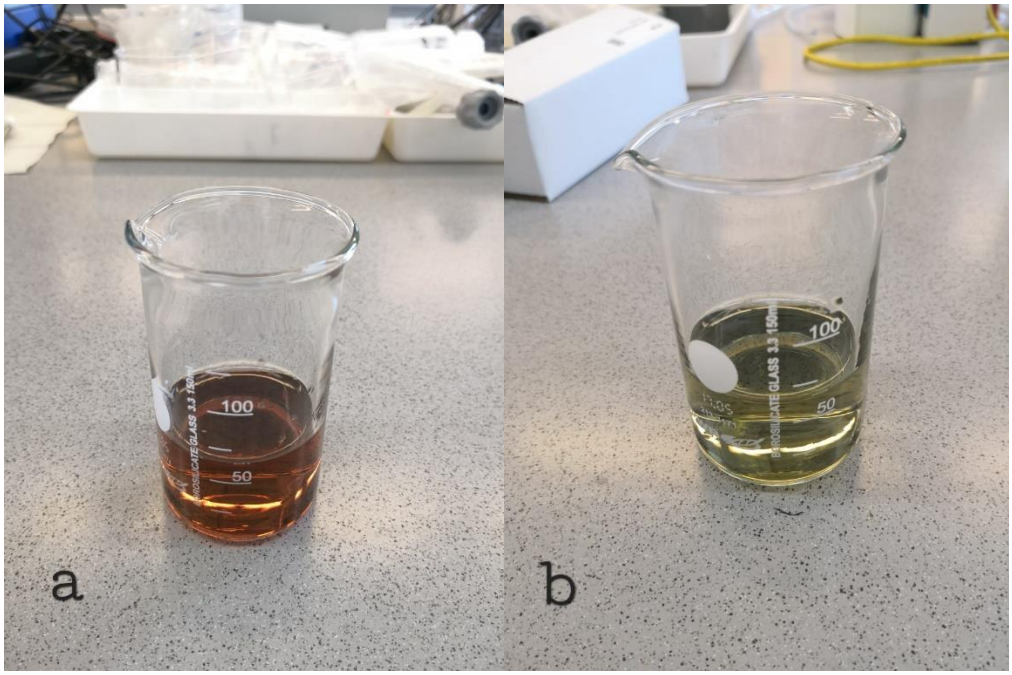

Figure 3-3. Resulting catalyst solutions of (a) NiFe and (b) NiCo.

3.1.3 Centrifuging

The final mixture was centrifuged at room temperature for five minutes at a speed of 8,000 revolutions per minute. Acceleration time was set at 2 minutes and the break at 3 minutes.

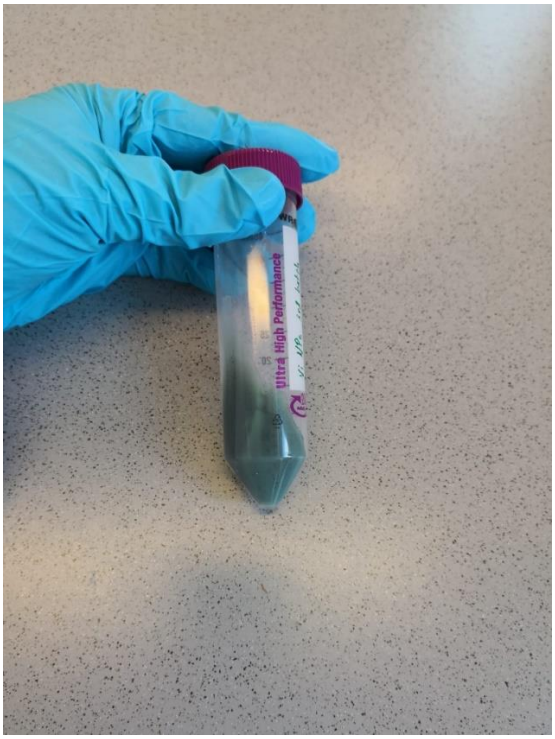

Figure 3-4. Centrifuged result.

3.1.4 Annealing

Once the centrifuge had been completed, the solid product was collected and placed in a crucible and then put into the oven for the annealing process. The annealing procedure lasted for six hours at an air temperature of 500 ° C, with a heating ramp of 10°C per minute. The annealing process took 6 hours and 30 minutes in total.

3.2 Characterization

3.2.1 Scanning electron microscopy (SEM)

The samples were analyzed using scanning electron microscopy (SEM, Zeiss supra 55 VP) to determine their morphology. The magnifications used were 1kX, 10kX, and 20kX, respectively. The accelerating voltage (or electron high tension, EHT) was maintained at 10 kV, and the secondary electron lens was utilized. Before conducting the tests, the samples were first reduced to a powdery consistency, and then a portion of that powder was placed on a sample holder. Next, the sample holder was inserted into the device, and then the SEM imaging was carried out.

3.2.2 Energy-Dispersive X-ray spectroscopy (EDX)

A Zeiss supra 55 VP scanning electron microscope equipped with EDX was utilized to carry out the energy dispersive X-ray microanalysis. This technique has the potential to provide information regarding the composition of the catalyst. For collecting the EDX data, 6 random data collection points were selected for each of the samples. The error limit for the device is known to be 2 percent, and any impurities that were found to have a concentration of less than 2% were excluded from the findings. The remaining components were collected and reported. The data from the EDX test was used to verify the catalyst sample composition.

3.2.3 X-ray powder diffraction (XRD)

A Bruker D8 A25 DaVinci X-ray Diffractometer with CuKα radiation was used to investigate the phase structure of the catalysts. After being ground into a powder, the catalyst was loaded into a Kapton sample holder to be inserted into the device.

The Kapton holder has two components: the sample holder and the black O-ring. Inside a fume hood, the holder was loaded with a sample that is in powder form and then covered with Kapton film. After that, the O-ring was placed to ensure that the film remained firmly in its position. A scissor was used to trim away any surplus Kapton film so that the film does not become lodged in the device.

The XRD apparatus had its setting predetermined at an angle ranging from 15–75 degrees for 60 minutes at 0.3-degree increments. Kapton holders were used as a means of mitigating danger because nanoparticles are regarded as hazardous and placed in the same category as carcinogenic and mutagenic substances.

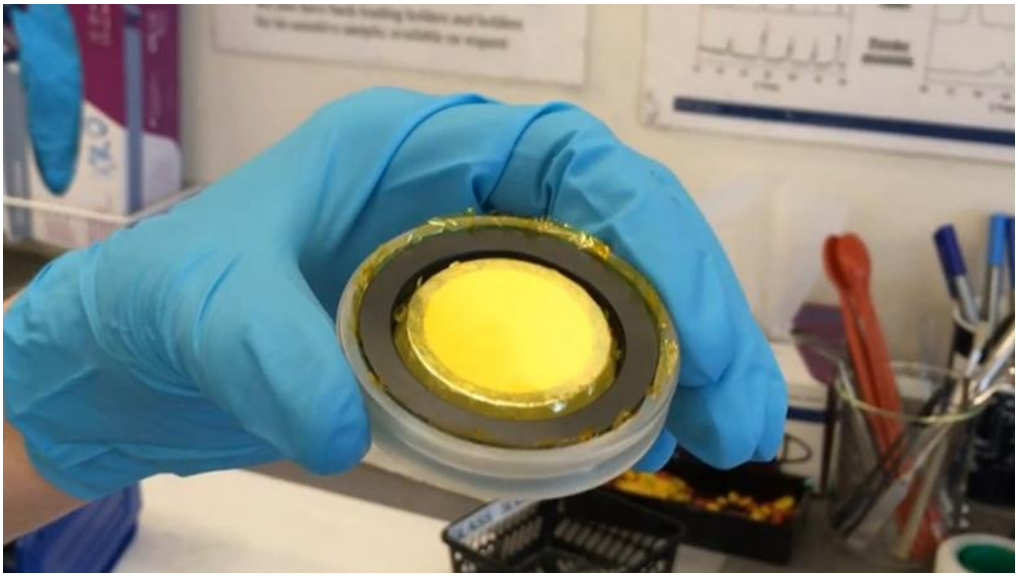

Figure 3-5. Kapton holder containing the sample.

3.2.4 Brunauer-Emmett-Teller (BET) and Barret-Joyner-Halenda (BJH) analysis

To determine catalyst physical surface area and pore volumes, BET surface area and BJH analysis were performed using a Micrometrics 3Flex 3500 Chemisorption Analyzer. Approximately 0.2 g of catalyst was used for each analysis. By utilizing N_2 adsorption, this equipment determines the surface area, the porous volume, and the average pore diameter of the sample. N_2 adsorption was measured at a temperature of -195.850°C.

N_2 gas was utilized for both the degassing process and the analysis.

Before any of the samples could be tested, they were each given a thorough drying to remove any moisture that may have been adsorbed on the surface.

A lint-free piece of paper and clean cotton gloves were used in the procedure of weighing the empty, clean, and dry test tube. After that, each sample was placed in its test tube, and the

combined weight of the test tube and sample was noted. This weight served as a baseline figure to determine whether or not the sample lost weight.

Table 3-2. Degas conditions set in software.

Sample preparation stage	Temperature (°C)	Ramp rate (°C/min)	Time (min)
1	90	10	60
2	250	10	480
3	25	10	10

The sample tube was then placed in the degassing device. The gas injection needle was inserted approximately 5 cm further down the sample tube, and a rubber cap was used to seal the sample tube. To initiate the flow of nitrogen, the nitrogen valve was twisted 1/8-1/4 of a turn counterclockwise. When the software for the degassing unit was launched, nitrogen began to flow through the system. The degas conditions that were configured in the software are outlined in Table 3-2.

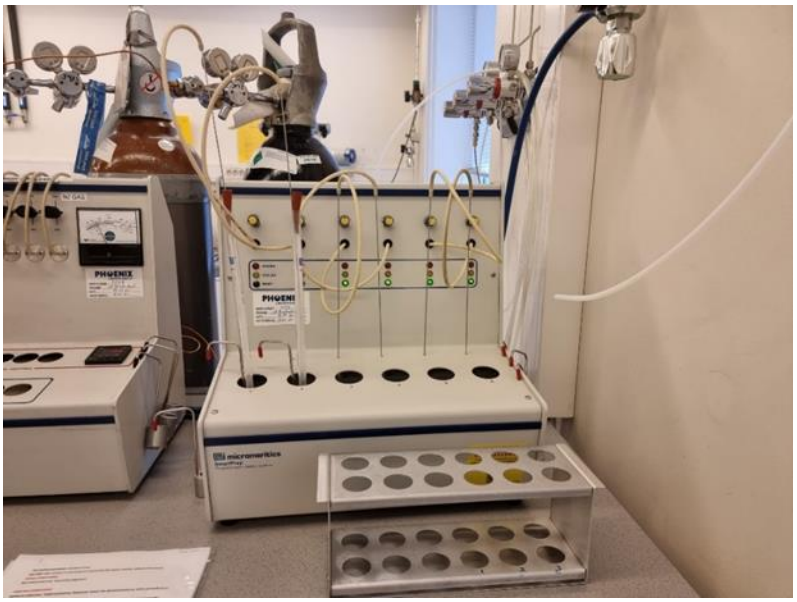

Figure 3-6. Degas setup.

After the degas stage, samples were weighted again to acquire the weight of dry samples.

For running the analysis, the sample tubes were covered with isothermal jackets to avoid temperature gradients within the tubes. The calculated weight of the samples was entered into the software and the use of the isothermal jacket option was marked. The analysis condition was set on the BJH pore size distribution.

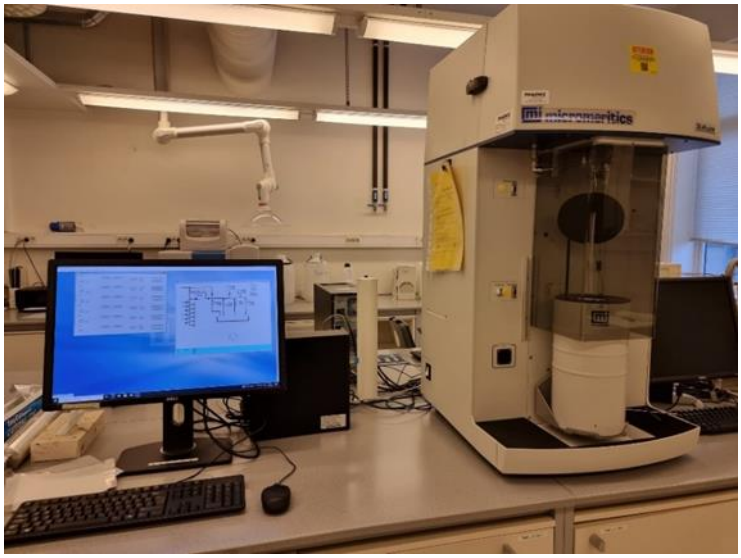

Figure 3-7. Micrometrics 3Flex 3500 Chemisorption Analyzer.

3.3 Catalyst ink preparation

For investigating the electrochemical characteristics, glassy carbon disk electrodes were used. These electrodes were polished prior to loading the samples on them. There were two phases to the polishing process. The electrodes were polished using a 5-micrometer aluminum oxide solution that was applied to a nylon polishing pad during the first stage. After polishing for one minute, the electrode was washed with distilled water. This process was repeated five times. On a microcloth polishing pad, a solution of aluminum oxide with a particle size of 0.05 micrometers was employed for the second stage of the process. After polishing for one minute and rinsing with distilled water for a total of five times, the electrodes were sonicated in an ultrasonic bath for one minute, followed by a rinse in distilled water and then dried.

The creation of the ink was carried out in accordance with two different ink recipes.

After weighing and measuring 5 mg of the finely powdered catalyst for the first ink composition, it was placed in a vile made of glass. 750 µl of MilliQ water was added, followed by the addition of 50 µl of a Nafion 117 solution (Nafion 117 from Sigma-Aldrich ~5%) and then the vile was exposed to 2 minutes of sonication. After that, 250 µl of isopropanol was added, and the mixture was sonicated for an additional two minutes. Because of the instability of this ink recipe while being analyzed, a second ink composition was used.

For the second ink composition, ten milligrams of the finely powdered catalyst were measured out, given a weight, and then placed in a vile made of glass. After adding 1 ml of ethanol, the

mixture was sonicated for a total of 2.5 minutes. After that, 50 μl of Nafion solution was added, and the mixture was sonicated for an additional 2.5 minutes.

After the inks had been prepared, 5 microliters of each ink were put onto the glassy carbon disk electrode and allowed to dry until they formed a thin layer over the surface of the electrode. In total, 63 inks were prepared for this work. Seven different samples (Table 3-1), three different synthesis attempts to assure repeatability, and three inks were created from each sample for electrochemical characterization.

3.4 Electrochemical measurements

Rotating disk electrode (RDE) measurements were performed using an electrochemical cell made of Teflon of conventional design, containing a counter electrode, a reference electrode, and a glassy carbon working electrode with a uniformly applied layer catalyst on its surface. All measurements were performed using a rotation rate of 1600 rpm at room temperature. Specifications of the electrochemical equipment used are provided in Table 3-3.

Table 3-3. Setup specifications for electrolyte preparation.

Component	Detail
Rotator and Motor	AFMSRCE, Pine Research MSR Rotator
Cell	Teflon electrochemical cell
Working electrode	AFE3T050GC, Pine Research, 5 mm OD glassy carbon disk electrode (covered with catalyst)
Counter electrode	Platinum
Reference electrode	Hg/HgO, Pine Research
Analysis software	IviumSoft

The electrolyte used was 250 ml of potassium hydroxide at a concentration of 1.0 M. The electrolyte was subjected to nitrogen purging for thirty minutes prior to measurements in order to remove all traces of free oxygen.

Figure 3-8. The RDE setup.

3.4.1 Electrochemical Impedance Spectroscopy

For this characterization, starting potentials of 0.8, 0.7, and 0.6 V were used in the range of 100kHz-0.1Hz and an amplitude of 0.005 V. The frequency setting was set on single sine with a total of 31 frequencies to be measured with 5 frequency decades between each point.

From the values obtained from Z', Z'' graphs, the average ohmic resistance of the system was obtained for each sample. Fitted by reducing 15% (85% was used, rewrite) of it as device resistance and applied as IR feedback during other electrochemical measurements.

3.4.2 Linear Sweep Voltammetry

In this work, LSV was performed at potential windows ranging from 0.2 to 0.8 V vs. Hg/HgO, with a scan speed of 1 mV/sec. All LSV measurements were carried out three times. As mentioned above, the IR feedback was applied in order to remove the ohmic drop.

3.4.3 Cyclic Voltammetry

In this study, cyclic voltammetry was carried out between a lower potential of 0.2 and an upper potential of 0.8 V vs. Hg/HgO. Prior to measurements, 50 CVs are performed at a scan rate of 100 mV/sec to treat the catalyst.

Subsequently, about 10 cyclic voltammograms were performed at a variety of scan rates in a small potential region with no Faradaic currents. This potential range varies slightly with each sample. Slow scan rates were originally used in the first CV sequence (100, 10, 20, 30, 50, 100, 200, 400, and 100 mv/s), but were later modified as the relatively long testing time led to unstable catalyst performance. The final sequence of scan rates performed was: 100, 50, 100, 150, 200, 250, 300, 350, and 400 mV/s.

Chapter 4

Results and Discussions

4.1 Characterization

4.1.1 Scanning electron microscopy

SEM was used to investigate the surface morphological properties of the manufactured catalysts. SEM images of the samples are shown in Table 4-1. The first row of the table shows SEM images of nickel nanoparticles. The obtained Ni nanoparticles have a uniform distribution, and the agglomerations have the appearance of crystals.

The SEM images of the Ni_3Fe_1 synthesized catalysts revealed that they were predominantly granular and composed of nanostructured grains (50 nm to several hundred nm). Compared to Ni_3Co_1, the grain dispersion of Ni_3Fe_1 was significantly higher.

Table 4-1. SEM images of the samples

Sample	**1kX**	**10kX**	**20kX**
Ni	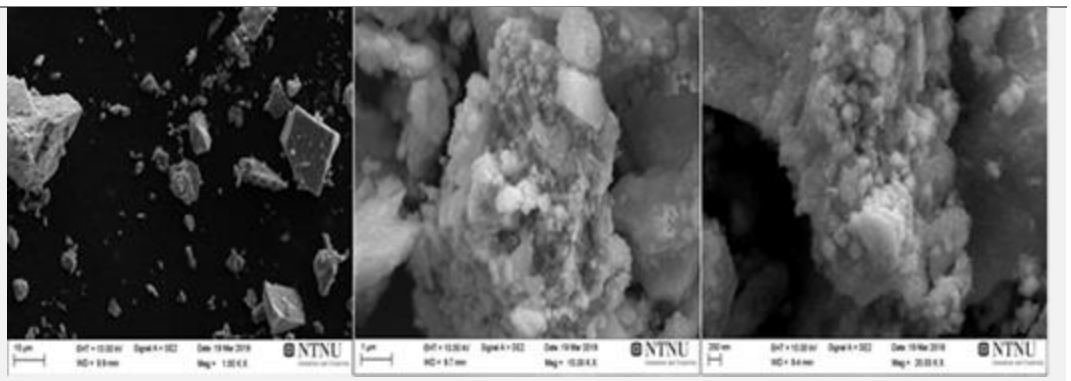		
Ni_1Co_1	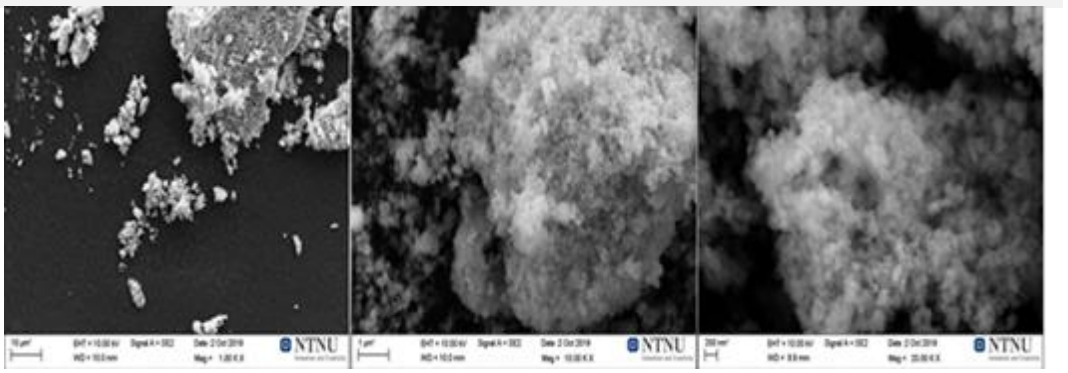		

Ni_1Co_3

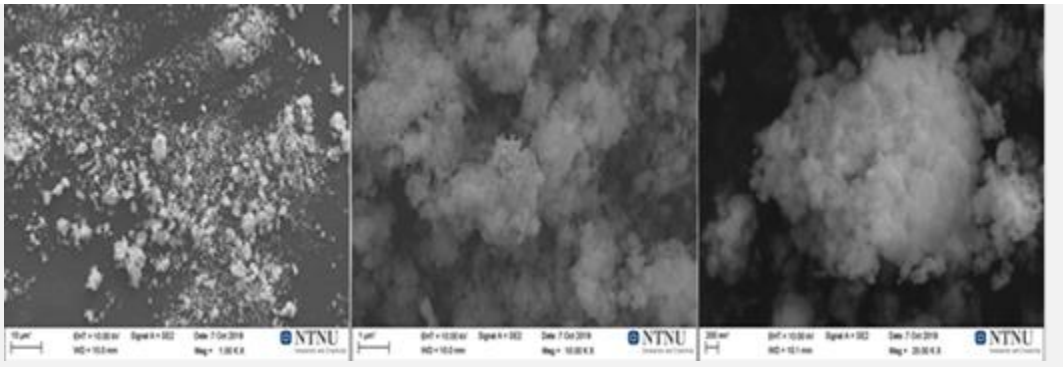

Ni_3Co_1

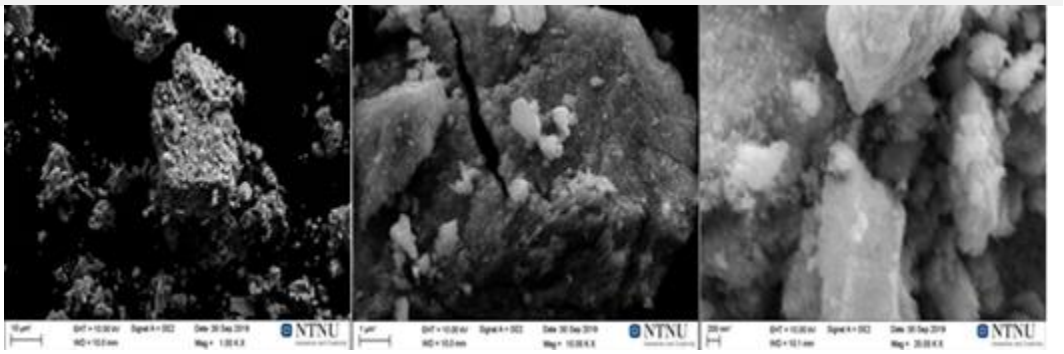

Ni_1Fe_1

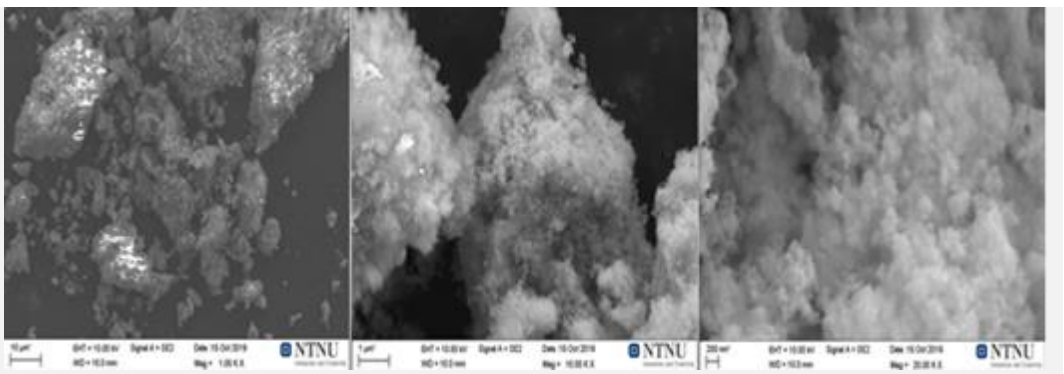

Ni_1Fe_3

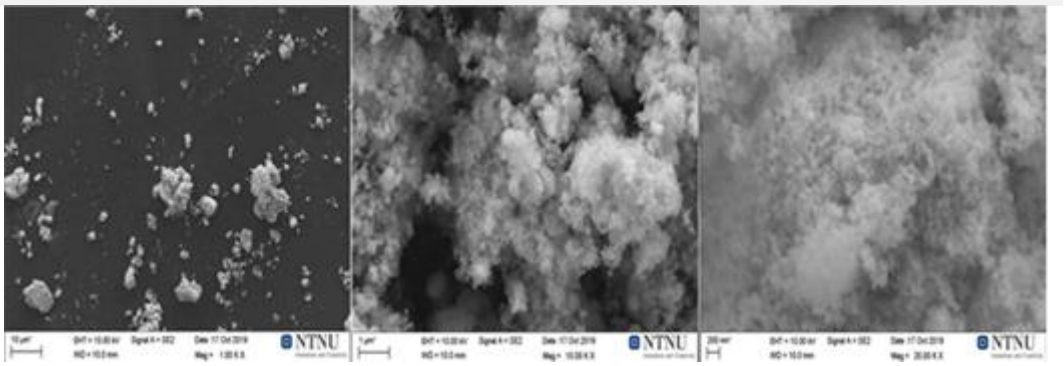

Ni_3Fe_1

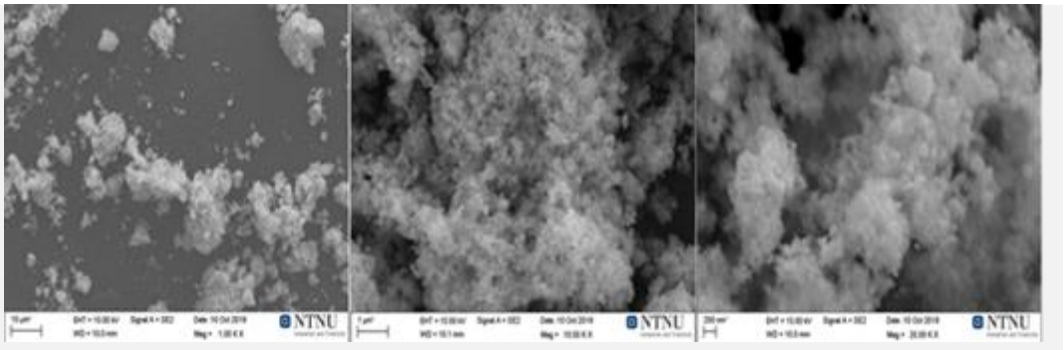

Because of the dense agglomeration of Ni nanoparticles, the particles appear to be clusters of nanoparticles. This SEM image can be used to determine the size of polycrystalline particles. Because of the high surface energy, surface tension, and magnetic properties of nickel, ultrafine nickel nanoparticles agglomerate, resulting in larger nanoparticles. The nanoparticles have higher catalytic activity due to the large surface area provided by their small size. The presence of these agglomerations coupled with the results of EDX confirms the formation of the Ni nanoparticles.

Pores of spherical shape were found on the Ni_1Fe_3 surface. Ni_1Fe_1's surface was covered in clustered shapes at the same time. As opposed to other catalysts, the surface area of Ni_3Fe_1 has a smaller surface area due to the formation of spherical shapes between the pores. The nickel-based catalysts were well synthesized into the same shape.

Spherical-shaped pores filled the surface of Ni_1Co_3. Meanwhile, large cubic shapes covered Ni_3Co_1's surface. In contrast, the bulk catalyst of Ni_1Co_1 has numerous spherical shapes formed between the pores and has more of an agglomerated form.

4.1.2 Energy-Dispersive X-ray spectroscopy

EDX analysis was used to determine the composition of the synthesized nickel-based catalysts. Three samples were analyzed for each catalyst using EDX. The composition of nickel-based catalysts is listed in Table 4-2.

Table 4-2 Sample compositions from EDX measurements in Atomic%.

Sample	Ni	Co	Fe	K	Ni:Co ratio	Ni:Fe ratio
Ni	96.69±1.55[1]	-	-	3.31±4.21	-	-
Ni_1Co_1	54.43±2.15	43.13±4.04	-	2.44±1.96	1.26±0.10	-
Ni_1Co_3	29.27±2.99	65.35±0.55	-	5.38±2.88	2.23±0.10	-
Ni_3Co_1	75.68±0.94	22.54±2.23	-	1.78±2.22	3.36±0.10	-
Ni_1Fe_1	45.56±6.72	-	48.72±5.98	5.72±4.49	-	1.07±0.19
Ni_1Fe_3	32.79±5.71	-	65.12±5.89	2.09±0.90	-	1.99±0.20

[1] Based on standard deviation calculation, $\sigma = \sqrt{\frac{1}{N}\sum_{i=1}^{N}(x_i - \mu)^2}$, where N is the number of repeats, μ is the mean and x_i the individual experimental values

Ni_3Fe_1	70.60±6.32	-	20.86±1.82	8.54±8.09	-	3.38±0.12

Figure 4-1 shows the EDX results of Ni nanoparticles. The elemental analysis reveals an average nickel concentration of 96.69% in the catalyst powder's structure. Potassium makes up the remainder of the Ni catalyst's composition at a very small percentage. This is likely related to the potassium hydroxide solution that was used throughout the synthesis procedure. Table 4-1 displays the results of an Ni EDX analysis performed on the synthesized catalysts. The relative Ni content of each sample was greater than 90.75%, with Ni atoms having a concentration of 100% on the second Ni catalyst sample.

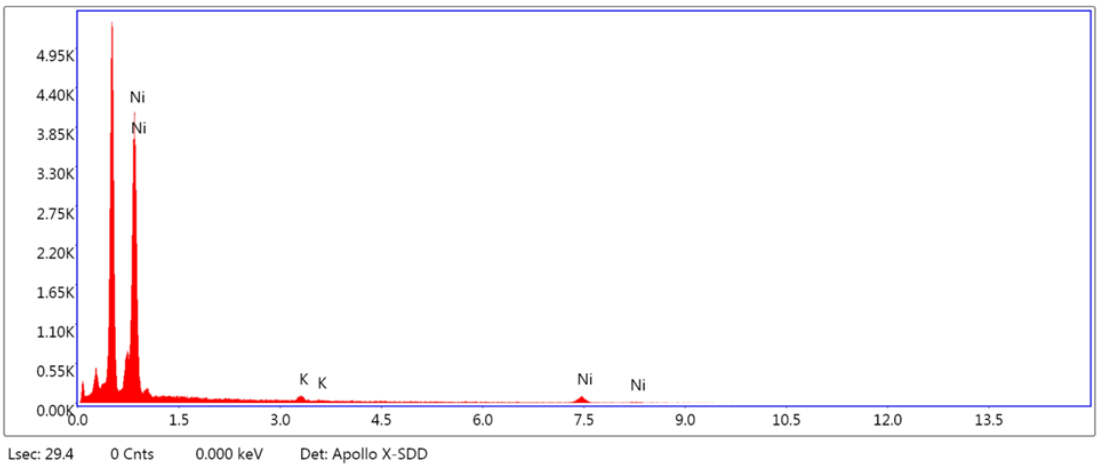

Figure 4-1. EDX result of Ni nanoparticles.

The EDX spectrum of the Ni_1Co_1 catalyst is shown in Figure 4-2 (a), which provides information about the elemental make-up of the catalyst. The spectra provided evidence that the catalyst contained elements of nickel, cobalt, and potassium. The experimental ratio of Ni_1Co_1 was determined by EDX and is summarized in Table 4-2. The elemental analysis reveals that the structure of the catalyst powder contains a moderate amount of nickel, with an average of 54.43% of the element. The remaining components of the catalyst are cobalt (with an average percentage of 43.13%) and potassium (with a low percentage).

In addition to this, the atomic ratio of nickel to cobalt for each sample is presented in Table 4-2. Table 4-2 reveals a moderate increase in Ni/Co molar ratio, which may be connected to a certain degree of nickel agglomeration. The experimental result shows a 26% increase in the ratio when compared to the intended ratio for this type of catalyst.

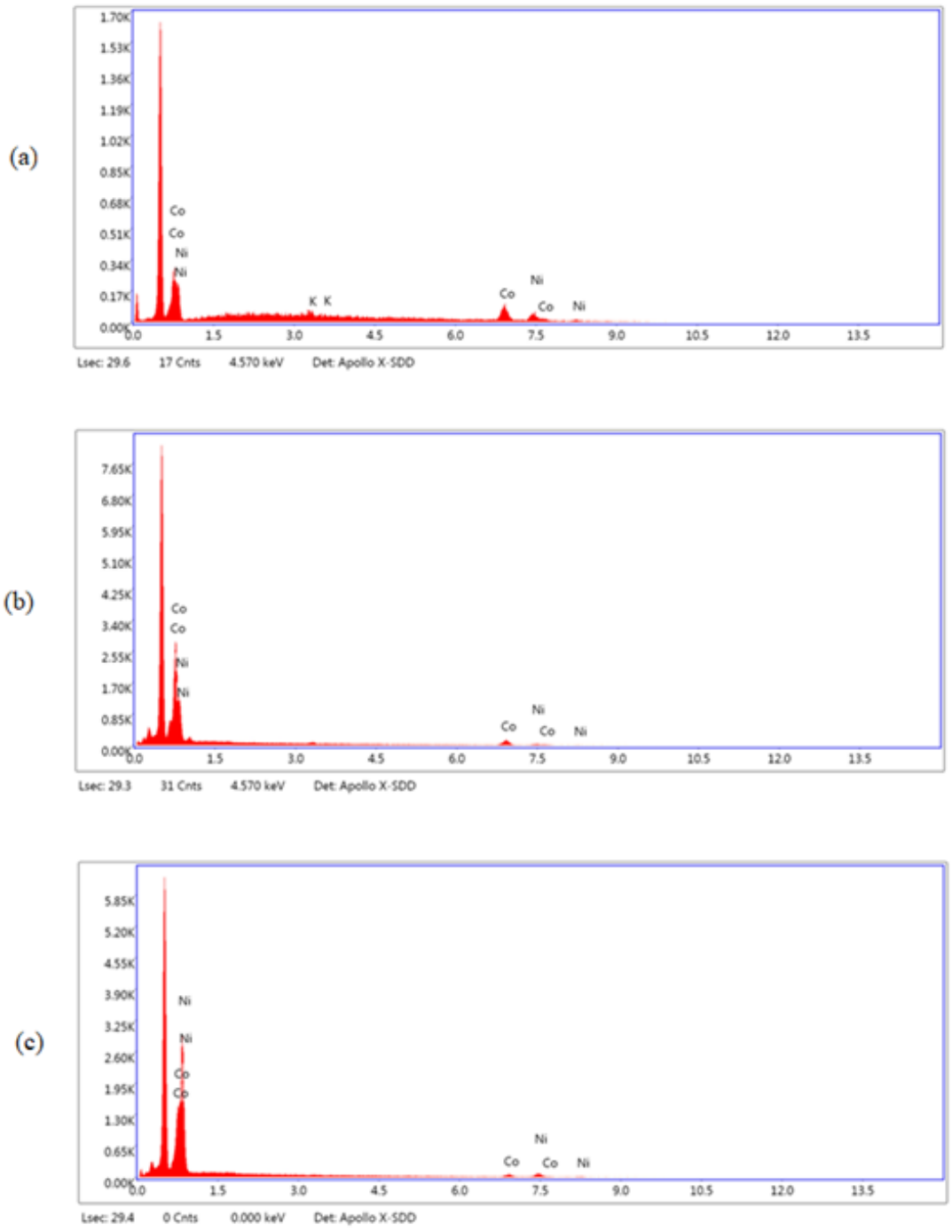

Figure 4-2. EDX results of (a) Ni_1Co_1, (b), Ni_1Co_3, (c) Ni_3Co_1.

Figure 4-2 (b) depicts the EDX spectra of the Ni_1Co_3 catalyst. The spectra supported the hypothesis that the catalyst contained Ni, Co, and K. Table 4-2 shows the experimental ratio of Ni_1Co_3 determined by EDX. The elemental analysis reveals that the structure of the catalyst powder contains a significant amount of cobalt, with an average of 65.35%. The remaining components of the catalyst are nickel (29.27%) and potassium, with a relatively small weight percentage.

The theoretical and experimental Ni and Co values in the catalysts differ to some extent. The nickel-cobalt ratio in the catalysts shows a decrease of approximately 25.6% compared to the stoichiometric one. The first sample had the highest nickel to cobalt ratio and the highest weight percentage of potassium. According to the explanation, the potassium hydroxide solution used in the synthesis process may be responsible for the experimental potassium composition found in the catalysts.

Figures 4-2 (c) depict the EDX spectrum of a Ni_3Co_1 catalyst. The elemental composition of the catalyst was determined through the investigation that yielded the spectrum. Spectra verified the existence of Ni, Co, and K components in the catalyst. Table 4-2 presents the EDX-determined experimental ratio. The elemental analysis reveals an average nickel concentration of 75.68% in the structure of the catalyst powder. The remainder of the catalyst consists of cobalt at an average weight percentage of 22.54% and potassium at a relatively low weight percentage.

The experimental values of Ni and Co in catalysts were not significantly different from their theoretical values. It indicates that the ratio of Ni to Co in the synthesized catalysts is nearly stoichiometric with only a 12% increase.

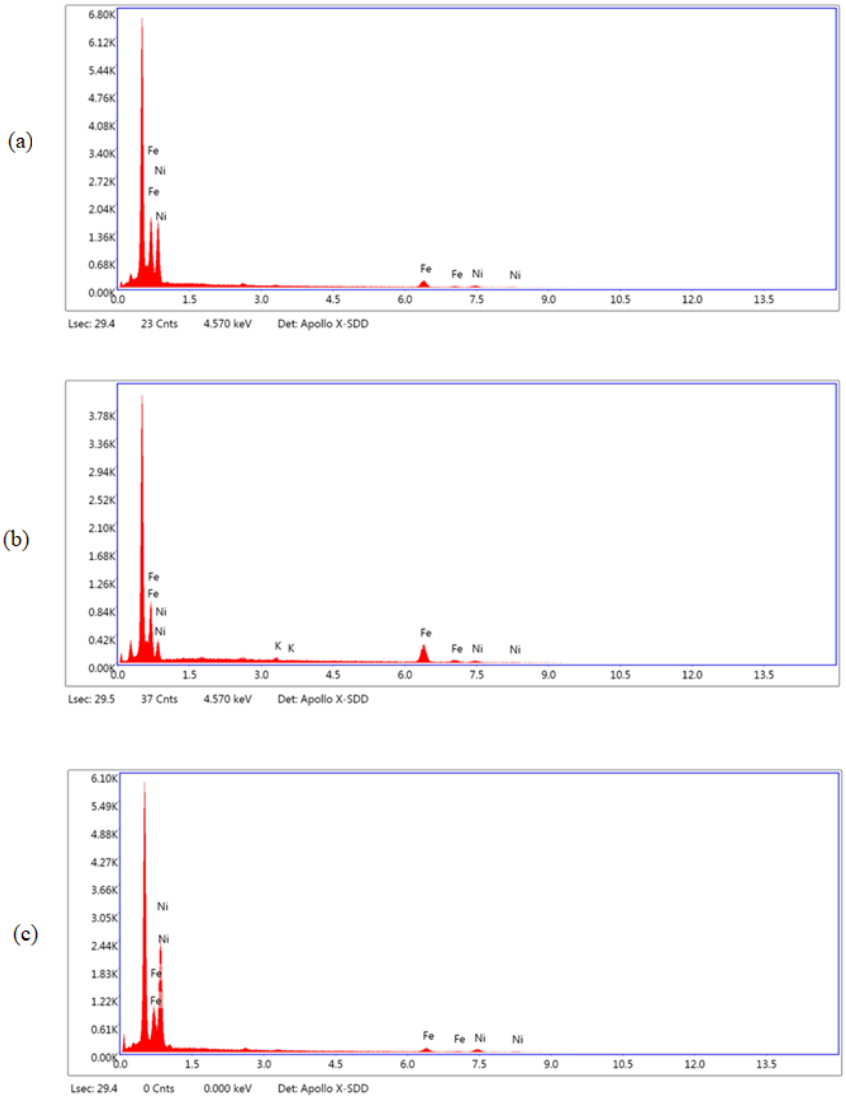

Figure 4-3. EDX results of (a) Ni_1Fe_1, (b) Ni_1Fe_3 and (c) Ni_3Fe_1.

Figure 4-3 (a) illustrates the EDX spectra of the Ni_1Fe_1 catalyst. The spectra demonstrated that the catalyst contained Ni, Fe, and K components. Table 4-2 lists the experimental ratio of Ni_1Fe_1 determined by EDX. The elemental analysis reveals that the structure of the catalyst powder comprises a moderate amount of nickel, with an average of 45.56% of the element. The remaining components of the catalyst are iron (48.72%) and potassium, with a low weight percentage.

Table 4-2 also shows the atomic ratio of Ni to Fe for these samples, which is 1.07 on average. The first sample had the highest proportion of Fe; it also had a high weight percentage of potassium (6.19%), which might be attributed to the more equal distribution of potassium on the catalyst's surface.

The EDX spectrum of a Ni_1Fe_3 catalyst can be observed in Figure 4-3 (b). Spectra provided conclusive evidence that the catalyst contained elements of nickel, iron, and potassium. The experimental ratio of Ni_1Fe_3, as determined by EDX, is detailed in Table 4-2. In the structure of the catalyst powder, the elemental analysis reveals that there is an average nickel concentration of 32.79%. Iron makes up the remaining part of the catalyst at an average weight percentage of 65.12%, while potassium makes up the remaining part at a relatively low weight percentage.

The theoretical and experimental values of nickel and iron found in catalysts differ from one another by about 33.6% in their molar ratio. It suggests that the ratio of nickel to iron in the synthesized catalysts is not stoichiometric.

The composition of the Ni_3Fe_1 catalysts was determined by EDX analysis, as shown in Figure 4-3 (c). Three samples were used for each catalyst's EDX examination. The spectra revealed the existence of Ni, Fe, and K components in the catalyst. The experimental ratio determined by EDX is summarized in Table 4-2. The elemental analysis reveals a greater nickel content in the catalyst powder structure, with an average of 70.60%. The remainder of the catalyst composition is iron, with an average weight percentage of 20.86%, and potassium, with a lower weight percentage. However, a significant weight percentage of potassium (20.49%) was discovered in the third sample, which could be attributed to the presence of K on the bulk catalyst due to incomplete removal of potassium during the synthesis process.

Table 4-2 also shows the average atomic ratio of Ni/Fe for these samples. As shown, the Ni/Fe molar ratio of these samples shows a 12.6% larger value in comparison to the theoretical value.

4.1.3 X-ray powder diffraction

XRD was used to study the synthesized catalysts. It is worth noting that XRD can be used to examine the phase purity and crystal structure of nanoparticles. Figures 4-4 to 4-6 illustrate the XRD patterns of nickel and nickel-based catalysts. Counts per second are used to measure the intensity along the vertical axis, while the diffraction angle (2θ) is measured along the horizontal axis.

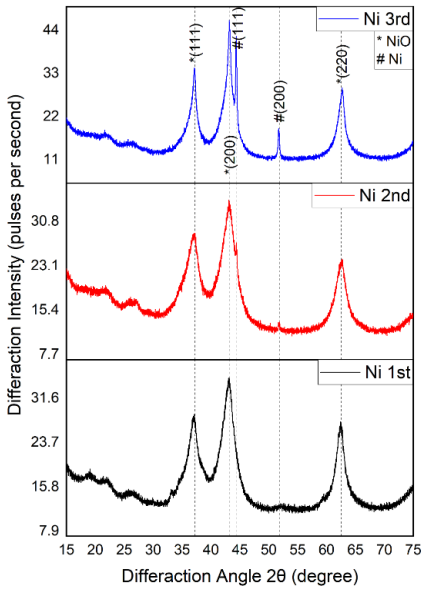

Figure 4-4. XRD pattern of Ni nanoparticles.

All of the catalysts exhibited diffraction peaks at 2θ = 44.1°, 51.3°, and 76.3°, corresponding to Ni(111), Ni(200), and Ni(220), respectively. XRD measurements, however, did not reveal any obvious oxide formation of the Ni nanoparticles in crystalline form. Although the presence of amorphous oxides cannot be determined by XRD.

Figure 4-5 depicts the XRD pattern of Ni_1Co_1, Ni_1Co_3, and Ni_3Co_1 samples, which confirmed the crystalline nature of the synthesized nickel-cobalt nanoparticles. Cobalt's simple cubic structure exhibits diffraction peaks at 2θ = 22.7°, 33.4°, 36.9°, 44.5°, 48.7°, 59.3°, and 65.7°, which correspond to the (111), (220), (311), (222), (422), (511) and (440) planes, respectively.

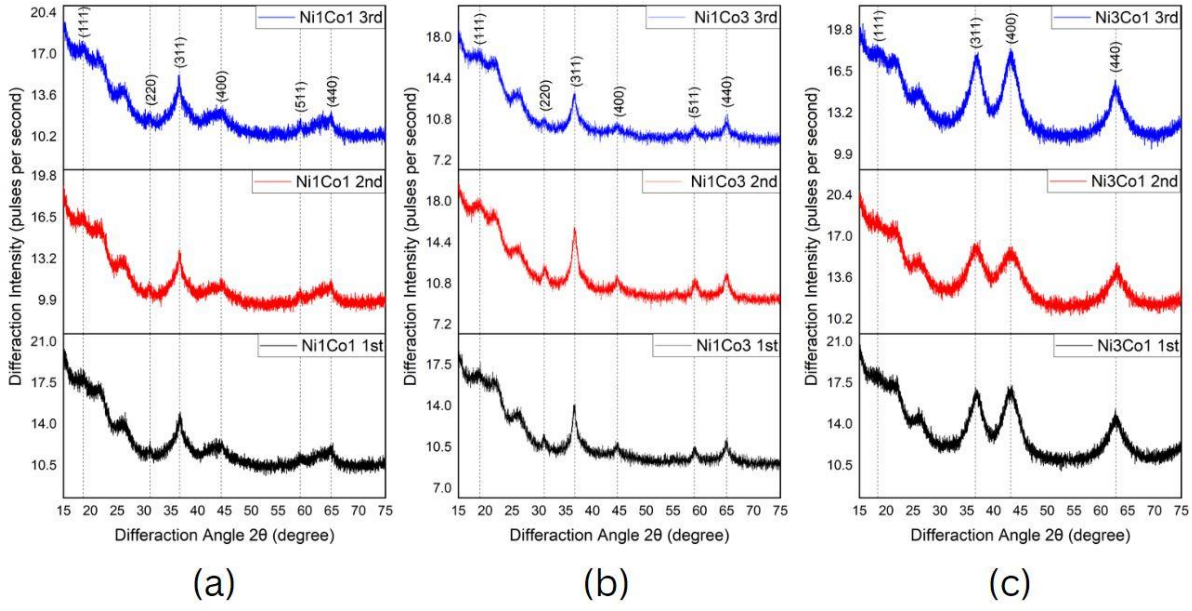

Figure 4-5. XRD pattern of (a) Ni_1Co_1, (b) Ni_1Co_3 and (c) Ni_3Co_1.

The XRD pattern of Ni_1Fe_3 nanoparticles is illustrated in Figure 4-6 (a). A major peak observed at approximately 2θ = 17.5 is attributed to particle diffraction from the (111) plane. A second peak is observed at 2θ = 65.37, corresponding to the (220) plane. The Ni_3Fe_1 crystal structure has a cubic structure. In Figure 4-6 (b), three broad, moderately intense peaks were observed at (311), (440), and (422) planes, confirming the formation of nanoparticles, with peaks at (113) and (205) indicating the formation of Fe_2O_3.

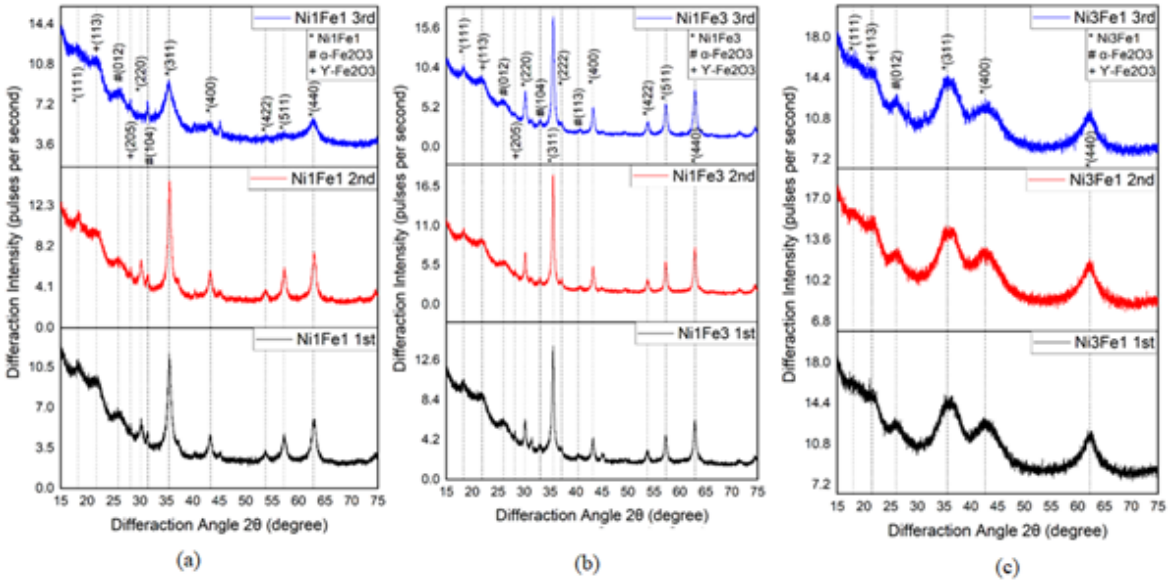

Figure 4-6. XRD pattern of (a) Ni_1Fe_1, (b) Ni_1Fe_3 and (c) Ni_3Fe_1.

The patterns demonstrate the formation of a cubic single-phase crystal structure. XRD did not detect any impurity peaks in the Ni_1Co_3 nanoparticles. Patterns of X-ray diffraction with broad peaks indicate that the particles of synthesized samples are in the nanometer range. Nickel diffraction peak intensity for Ni_1Co_3 and Ni_1Fe_3 was lower than that of Ni_3Co_1 and Ni_3Fe_1, and the half-peak width was wider.

4.1.4 BET and BJH analysis

The BET equation was used to compute the specific surface areas of the prepared catalysts, and the BJH equation was utilized to compute the pore volumes and average pore diameters. These equations and their calculations were pre-programmed into the device by the company. In Table 4-3, the textural characteristics of the catalysts are outlined.

Table 4-3. The textural characteristics of the catalysts.

Sample	BET Surface Area (m^2/g)	Langmuir Surface Area	BJH Desorption Cumulative Pores Volume (cm^3/g) *	BJH Desorption Average Pore Diameter (Å)
Ni	82.6198	652.4670	0.1578	49.9027
Ni_3Co_1	120.8166	830.5544	0.2213	49.7830
Ni_1Co_1	134.0750	2269.7005	0.4178	102.8513
Ni_1Co_3	153.4473	2763.2705	0.4869	107.0440
Ni_3Fe_1	162.4937	1995.8756	0.5065	101.3063
Ni_1Fe_1	46.0551	1620.6840	0.2487	199.4935
Ni_1Fe_3	26.5971	1670.8383	0.1985	244.1500

The comparison between the BET results makes it very clear that the Ni_3Fe_1 catalyst had the highest surface area of 162.4937 m^2/g compared to the other catalysts. According to the porosity size distribution that was calculated from desorption data using the BJH method, Ni_1Fe_3 has the largest desorption average pore diameter. Ni_3Co_1, on the other hand, has the lowest value. The XRD studies agreed with the findings of the BET surface-area measurement, which found that smaller crystallite sizes were associated with a larger surface area. Based on these findings, it appears that the presence of iron in Ni_1Fe_3 increases both the specific surface area and the pore volume. In light of this, the characteristics might be advantageous for the oxygen evolution reaction.

When compared to the surface area of the corresponding Ni_1Co_3, the surface area of Ni_1Fe_3 was significantly increased. This may be because the Ni_1Fe_3 sample's surface had a relatively dispersed porous structure.

4.2 Electrochemical measurements

4.2.1 Linear Sweep Voltammetry

In order to investigate the electrocatalytic activity of the nickel-based catalysts for OER, LSV measurements were carried out at a scan rate of 1 mV/s in an environment consisting of N_2-saturated 0.3 M of KOH. The LSVs of electrochemical oxygen evolution with nickel-based catalysts are shown in Figure 4-14. During the electrochemical investigation, it was noticed that the surface of the Ni_1Co_3 catalyst produced oxygen at a typically rapid rate. The electrochemical data reveals that Ni_1Co_3 has a reasonably high activity for the oxygen evolution reaction compared to other catalysts.

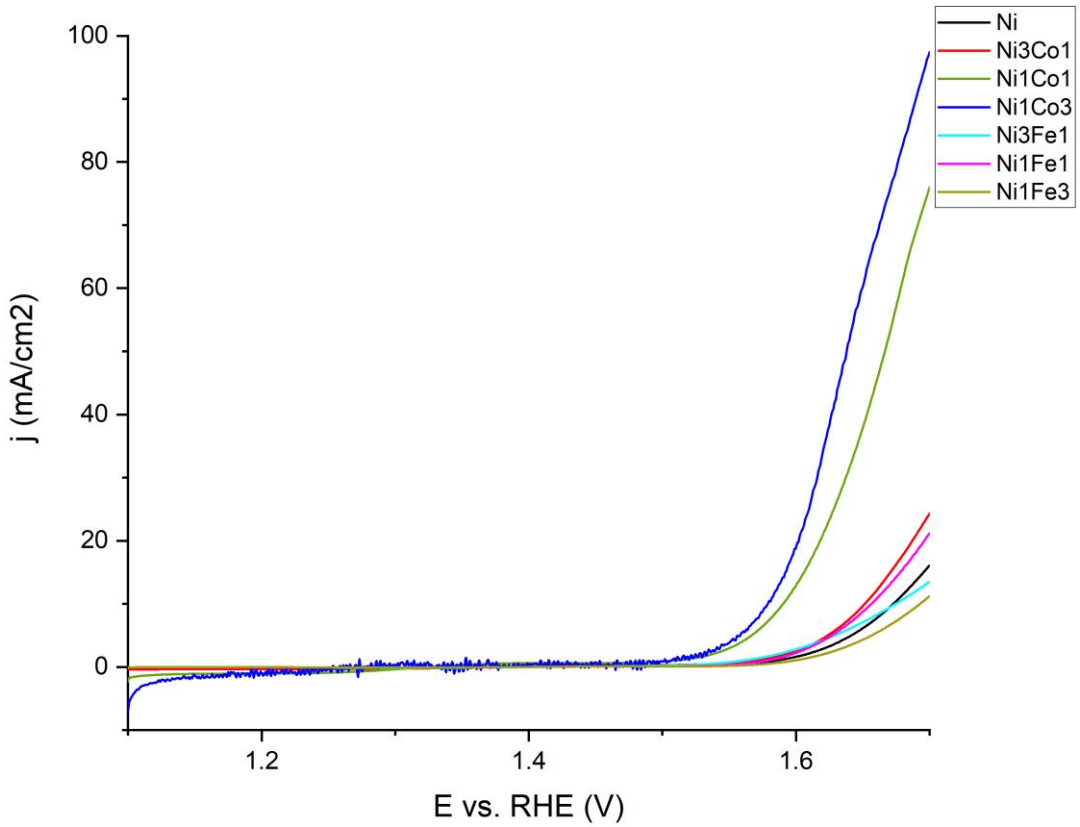

Figure 4-7. The LSVs measured with nickel-based catalysts (the geometrical area of the electrode's surface that was used, was measured as 1.196 cm^2).

As demonstrated, Ni_1Fe_3 showed the weakest performance among the tested samples. The OER with Ni_1Co_3 began at approximately 1.52 V and climbed abruptly to 1.7 V, whereas the OER with pure Ni began at 1.6 V and increased steadily.

At 1.6 V, the obtained current density was 25 mA/cm^2, whereas, at 1.7 V, it was close to 100 mA/cm^2, illustrating the improved performance of the Ni_1Co_3 catalyst. At a potential of 1.6 V, the Ni_1Co_1 exhibited a current density of 10 mA/cm^2 in contrast. At a potential of 1.6 V, a current density of 10 mA/cm^2 was measured for pure Ni. Ni_1Co_3 outperforms pure Ni and other catalysts substantially more effectively.

Importantly, Figure 4-7 demonstrates that the Ni oxidation peak prior to the onset of OER was substantially prevented. The substantially lower Ni oxidation peak compared to Ni_1Co_3, Ni_1Co_1, and Ni_3Co_1 indicates that OER active sites are more in the Ni-Co particles, rather than in Ni particles. As a result, the most effective substrate contains a Ni_1Co_3 catalyst. This data indicates that OER occurs faster in the presence of Ni_1Co_3 and Ni_1Co_1. It is also important to note that the presence of metallic Ni enables rapid electron transport within the nanoparticle, which is required for improved electrolysis performance.

Table 4-4. Relative average potential for each of the samples at 10 mA cm^{-2}.

Sample	**E vs. RHE (V)**
Ni	1.673
Ni_3Co_1	1.651
Ni_1Co_1	1.590
Ni_1Co_3	1.579
Ni_3Fe_1	1.675
Ni_1Fe_1	1.657
Ni_1Fe_3	1.693

4.2.2 Cyclic Voltammetry

Using a conventional three-electrode cell in an RDE set-up, the OER catalytic activity of nickel-based catalysts in O_2-purged 1 M of KOH electrolyte was investigated.

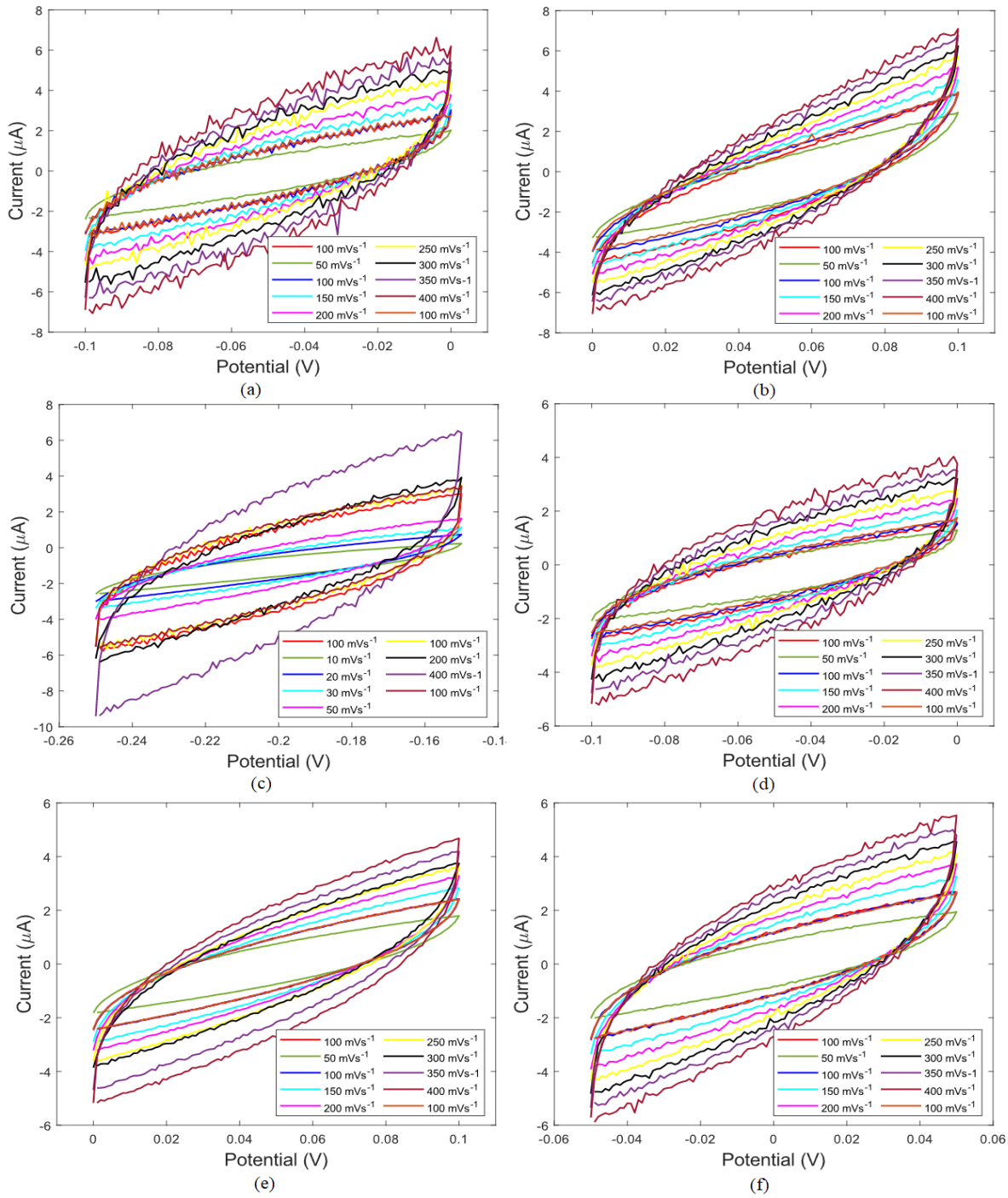

Figure 4-8. Cyclic voltammograms for oxygen evolution reaction.

Figure 4-8 shows that there is a direct transfer of electrons at the cathode based on the shape of the curves.

To estimate the actual catalytic activity, it is necessary to consider not only the kinetic parameters but also the overpotential of each catalyst at a constant current density under steady-state conditions. As shown in Figure 4-8, as the electrode potential was scanned to a higher

anodic value, the current density increased; in the instance of Ni_1Fe_3, a current density of 5.7 μA was achieved at a scan rate of 400 mV/s.

4.2.3 Electrochemical Impedance Spectroscopy

Ohmic resistance results are listed in Table 4-4, achieved by IviumSoft software. It provides access to a wide range of analysis and evaluation methods for data. All common electrochemical techniques are built into IviumSoft, as is automatic optimization for fast, sensitive operation and streamlined data analysis. IviumSoft is utilized to configure the EIS measurement. There are four distinct impedance methods that can be chosen depending on the needs of the measurement. EIS interfacial characteristics depend on the environment in which charge transfer happens, the composition of the electrolyte, and the electrode. Table 4-4 lists the results of the EIS for each catalyst.

Table 4-4. Ohmic resistance results.

Sample	**1st Ink (ohm)**	**2nd Ink (ohm)**	**3rd Ink (ohm)**	**Average ohmic resistance (ohm)**
Ni 1st batch	6.4045	5.3819	6.6393	6.1419
Ni 2nd batch	4.0755	3.9839	3.9055	3.9883
Ni 3rd batch	4.4928	3.9160	3.9344	4.1144
Ni total				**4.7482**
Ni_3Co_1 1st batch	5.0779	4.9810	5.3176	5.1255
Ni_3Co_1 2nd batch	5.7395	5.6100	5.8202	5.7232
Ni_3Co_1 3rd batch	5.3140	5.2876	5.4559	5.3525
Ni_3Co_1 total				**5.4004**
Ni_1Co_1 1st batch	4.4291	4.2190	5.1691	4.6057
Ni_1Co_1 2nd batch	5.3927	4.4047	5.9061	5.2345
Ni_1Co_1 3rd batch	3.9862	4.7835	5.5324	4.7674
Ni_1Co_1 total				**4.8692**
Ni_1Co_3 1st batch	4.5084	5.3357	5.6981	5.1807
Ni_1Co_3 2nd batch	5.6502	7.9169	6.5671	6.7114

Ni_1Co_3 3rd batch	7.8305	6.7584	6.1243	6.9044
Ni_1Co_3 total				**6.2655**
Ni_3Fe_1 1st batch	8.8173	10.4635	10.4323	9.9044
Ni_3Fe_1 2nd batch	13.3676	7.3216	7.6746	9.4546
Ni_3Fe_1 3rd batch	6.2268	11.2512	6.0455	7.8412
Ni_3Fe_1 total				**9.0667**
Ni_1Fe_1 1st batch	8.0708	6.5076	5.2448	6.6077
Ni_1Fe_1 2nd batch	5.8829	5.3278	6.7521	5.9876
Ni_1Fe_1 3rd batch	8.6731	8.9811	7.1969	8.2837
Ni_1Fe_1 total				**6.9597**
Ni_1Fe_3 1st batch	10.3165	6.4784	5.0830	7.2926
Ni_1Fe_3 2nd batch	5.1697	4.8150	5.5074	5.1640
Ni_1Fe_3 3rd batch	11.7782	5.5599	5.8721	7.7367
Ni_1Fe_3 total				**6.7311**

Figure 4-16 shows the Z', Z'' sample graph based on Ni EIS results and the point that the data was read to measure the ohmic resistance.

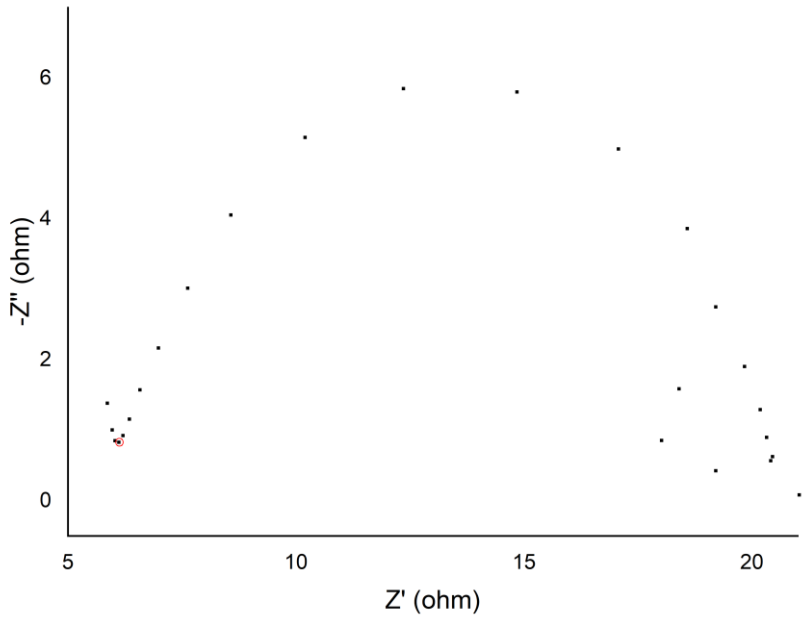

Figure 4-9. Z', Z'' sample graph based on Ni EIS results.

The values read from the graphs are the lowest points at the beginning of the graph's curve that is marked with a red circle in the Z', Z'' graph, shown in Figure 4-16.

The high frequency intercept of the reed axis is taken as the lowest point in the high frequency region. This value was then considered as ohmic resistance.

4.2.4 Electrochemical surface area (ECSA)

In-depth electrochemical studies in alkaline solutions were conducted to examine the electrocatalytic performance of the electrodeposited films for OER. By measuring the electrochemical capacitance of the electrode–electrolyte interface in the double-layer regime, the electrochemically active surface areas of the catalysts were computed. From the non-faradaic double-layer region, the capacitance of a double-layered electrode (C_{dl}) was computed, and the capacitive current (i_C) was estimated. This current is caused by charge accumulation as opposed to chemical reactions or charge transfer, and it is directly proportional to the scan rate.

Table 4-5. ECSA results.

Sample	**Double-Layer Capacitance (F)**	**Electrochemical Active Surface Area (cm^2)**	**Roughness Factor**
Ni	9.5544×10^{-6}	0.4777	2.4373
Ni_3Co_1	6.8384×10^{-6}	0.3419	1.7445
Ni_1Co_1	5.5162×10^{-6}	0.2758	1.4072
Ni_1Co_3	9.7137×10^{-6}	0.4857	2.4780
Ni_3Fe_1	4.8296×10^{-6}	0.2415	1.2320
Ni_1Fe_1	5.8196×10^{-6}	0.2910	1.4846
Ni_1Fe_3	6.4565×10^{-6}	0.3228	1.6571

According to McCrory et al., the C_s value for turning the C_{dl} to ECSA was 0.02 mF/cm^2 [47].

The value for turning ECSA to Roughness Factor was 0.196 cm^2, that was the surface area of the glassy carbon electrode which was used to run the RDE measurements.

Table 4-5 lists the ECSA and roughness factor (RF) of the various catalysts used in this study. To the best of our knowledge, these catalysts have never been reported as OER-active electrocatalysts. Lastly, the RF can be determined based on the estimate of ECSA. RF is

calculated by dividing the real area by the geometric area. The distribution, size, and morphology of electrocatalyst particles can be correlated with the roughness of a material. A rough surface is characterized by its structure's irregularity. Consequently, the RF value provides information regarding the geometry and distribution of active sites. A value of RF greater than one indicates a larger and more favorable absorption area. In this study, all catalysts with RF values greater than one have favorable adsorption surface areas.

It was observed that among all catalysts, RF became highest for Ni_1Co_3 (2.4780). Pure Ni still exhibited the second-highest RF (2.4373), but the RF value for Ni_3Co_1 became the third highest (1.7445), even though it is slightly higher than those of Ni_1Fe_3 (1.6571) and Ni_1Fe_1 (1.4846). Ni_3Fe_1 (0.2415 cm^2) and Ni_1Co_1 (0.2758) showed the lowest ECSA values, respectively. It was observed that RF became least for Ni_3Fe_1 (1.2320).

Ni_1Co_3, Ni, and Ni_3Co_1 were found to have the best RF performance of all the catalysts tested for electrochemical performance. Consequently, these catalysts create a larger and more favorable adsorption area.

In particular, Ni_1Co_3 had the highest value in ECSA and RF during OER. The electrochemical active surface area (ECSA) is one of the most important parameters for characterizing of an electrocatalyst because it establishes a link between the active catalytic sites of the material and its activity, which is useful for comparing and ranking catalysts [70]. The best way to characterize porosity and surface area is through physisorption measurement. The main drawback is that not all electrochemical labs have access to this technique, and depending on the actual specific surface area of the electrocatalyst, it may require up to several hundred milligrams of material to give reliable values. Evidence suggests that Ni_1Co_3 leads to the most durable surface owing to the formation of a bulk alloy of surface Co and underlying Ni atoms.

Chapter 5

Conclusion

In the current investigation, nickel-based was selected for use in alkaline electrolysis of water due to nickel's superior resistance to corrosion in highly concentrated alkaline medium, as well as its superior activity in this environment when compared to that of other metals. The low cost of alkaline electrolysis, along with the high power and versatility of PEM electrolyzers, is the goal of the process known as alkaline membrane water electrolysis.

OER catalysts that are active, affordable, and durable can be made from nickel and its alloys. The production of numerous nickel-based catalysts, including Ni_xCo_y, Ni_xFe_y, and Ni, was accomplished by reducing an aqueous mixture of metal precursors in the presence of sodium borohydride. In order to verify the reliability of the findings, each experiment was performed three times, and three different samples of each catalyst were used in each test. In addition to EDX analysis, which was used to determine the composition of the synthesized nickel-based catalysts, SEM was utilized in order to analyze the surface morphological features of the created catalysts. XRD was utilized in order to investigate the phase purity of nanoparticles as well as their crystal structures.

The results of the XRD tests were in agreement with the findings of the BJH and BET surface-area measurements, which discovered that a larger surface area was related to smaller crystallite sizes. When the surface area of the comparable Ni_1Co_3 was compared to the surface area of the Ni_1Fe_3, it was found that the Ni_1Fe_3 had a significantly larger surface area. This may be because the surface of the Ni_1Fe_3 sample had a very porous structure that was scattered throughout.

According to the findings of the LSV, the substrate with the greatest potential comprises a Ni_1Co_3 catalyst, and the rate of OER is accelerated in the presence of both Ni_1Co_3 and Ni_1Co_1. It is also crucial to note that the presence of metallic Ni provides for rapid electron transit within the nanoparticle, which is required for successful catalysis. This is something that is required in order for catalysis to take place.

In this work, calculations were used to determine the ECSA and the roughness factor (RF) of the various catalysts. To the best of our knowledge, this is the first time that these catalysts have been reported as OER-active electrocatalysts. Ahn and colleagues found that the hydrogen evolution reaction could be improved by using nickel metal with different physical properties,

such as thin films and nickel-based sheets that had been electrochemically coated on the carbon glass surface. For hydrogen evolution reactions using nickel dendrites, the results showed that increasing active surface area is directly proportional to increasing electrocatalytic activity [34].

To increase the stability of the water electrolysis reaction in an alkaline environment, nickel hydroxide nanoclusters were layered on nine substrates of intermediate metals, including copper, silver, gold, ruthenium, iridium, platinum, nickel, vanadium, and titanium. The overreaction potential of these metals was significantly reduced when nickel hydroxide was layered on top of them [35].

The RF value offers insight into the topology and distribution of active sites. If the value of RF is greater than one, it implies that the area of absorption is both larger and more favorable. According to the findings of this research, all of the catalysts with RF values higher than one possess advantageous adsorption surface areas.

RF was found to be the greatest for Ni_1Co_3 among all catalysts (2.4780). The RF value for pure Ni remained at the second-highest level (2.4373), but the RF value for Ni_3Co_1 was the third-highest level (1.7445), even though it is only marginally higher than the RF values for Ni_1Fe_3 (1.6571) and Ni_1Fe_1 (1.4846). Ni_3Fe_1 (with an ECSA value of 0.241 cm2) and Ni_1Co_1 (with an ECSA value of 0.2758) displayed the lowest ECSA values, respectively. It was noticed that RF decreased to its lowest level for Ni_3Fe_1 (1.2320).

Out of all of the catalysts that were examined for their electrochemical performance, it was discovered that Ni_1Co_3, Ni, and Ni_3Co_1 had the best RF performance. As a result, the adsorption area created by these catalysts is greater and more favorable than that created by the other catalysts tested.

In particular, Ni_1Co_3 had the highest values in ECSA and RF during OER, which suggests that Ni_1Co_3 leads to the most durable surface as a result of the formation of a bulk alloy of surface Co and underlying Ni atoms. This could be because Ni_1Co_3 leads to the formation of a bulk alloy of surface Co and underlying Ni atoms.

These findings, when combined with the straightforward synthesis process, earth-abundant availability of the raw ingredients, and the potential to fine-tune the catalytic efficiencies even further, make these compounds very attractive for use in a variety of energy-related practical applications.

References

1. Thielemann, T., S. Schmidt, and J.P. Gerling, *Lignite and hard coal: Energy suppliers for world needs until the year 2100—An outlook.* International Journal of Coal Geology, 2007. **72**(1): p. 1-14.
2. Paterson, R., et al., *World climate suitability projections to 2050 and 2100 for growing oil palm.* The Journal of Agricultural Science, 2017. **155**(5): p. 689-702.
3. Chi, J. and H. Yu, *Water electrolysis based on renewable energy for hydrogen production.* Chinese Journal of Catalysis, 2018. **39**(3): p. 390-394.
4. Stojić, D.L., et al., *Hydrogen generation from water electrolysis—possibilities of energy saving.* Journal of power sources, 2003. **118**(1-2): p. 315-319.
5. Ursua, A., L.M. Gandia, and P. Sanchis, *Hydrogen production from water electrolysis: current status and future trends.* Proceedings of the IEEE, 2011. **100**(2): p. 410-426.
6. Wang, M., et al., *The intensification technologies to water electrolysis for hydrogen production–A review.* Renewable and sustainable energy reviews, 2014. **29**: p. 573-588.
7. Zoulias, E., et al., *A review on water electrolysis.* Tcjst, 2004. **4**(2): p. 41-71.
8. LeRoy, R., *Industrial water electrolysis: present and future.* International Journal of Hydrogen Energy, 1983. **8**(6): p. 401-417.
9. Bernt, M., et al., *Analysis of gas permeation phenomena in a PEM water electrolyzer operated at high pressure and high current density.* Journal of The Electrochemical Society, 2020. **167**(12): p. 124502.
10. Siracusano, S., et al., *New insights into the stability of a high performance nanostructured catalyst for sustainable water electrolysis.* Nano Energy, 2017. **40**: p. 618-632.
11. Lenivova, V., *Potential development of renewable hydrogen imports to European markets until 2030.* 2022.
12. Santos, D., et al., *Platinum–rare earth electrodes for hydrogen evolution in alkaline water electrolysis.* International journal of hydrogen energy, 2013. **38**(8): p. 3137-3145.
13. Chen, Y.W.D. and R.N. Noufi, *Electrodeposition of nickel and cobalt oxides onto platinum and graphite electrodes for alkaline water electrolysis.* Journal of the Electrochemical Society, 1984. **131**(4): p. 731.
14. Jain, I., *Hydrogen the fuel for 21st century.* International journal of hydrogen energy, 2009. **34**(17): p. 7368-7378.
15. Sharma, S. and S.K. Ghoshal, *Hydrogen the future transportation fuel: From production to applications.* Renewable and sustainable energy reviews, 2015. **43**: p. 1151-1158.
16. Sinigaglia, T., et al., *Production, storage, fuel stations of hydrogen and its utilization in automotive applications-a review.* International journal of hydrogen energy, 2017. **42**(39): p. 24597-24611.
17. Colozza, A.J. and L. Kohout, *Hydrogen storage for aircraft applications overview*. 2002.
18. Felseghi, R.-A., et al., *Hydrogen fuel cell technology for the sustainable future of stationary applications.* Energies, 2019. **12**(23): p. 4593.
19. Kundu, P. and K. Dutta, *Hydrogen fuel cells for portable applications*, in *Compendium of hydrogen energy*. 2016, Elsevier. p. 111-131.
20. Wang, D., et al., *Quantifying the flexibility of hydrogen production systems to support large-scale renewable energy integration.* Journal of Power Sources, 2018. **399**: p. 383-391.
21. Schmalensee, R., *Competitive Energy Storage and the Duck Curve.* The Energy Journal, 2022. **43**(2).
22. Schoenung, S.M. and J.O. Keller, *Commercial potential for renewable hydrogen in California.* International Journal of Hydrogen Energy, 2017. **42**(19): p. 13321-13328.
23. Kosowatz, J., *Energy storage smooths the duck curve.* Mechanical Engineering, 2018. **140**(06): p. 30-35.

24. Wang, Q., et al., *Mitigation strategy for duck curve in high photovoltaic penetration power system using concentrating solar power station.* Energies, 2019. **12**(18): p. 3521.
25. Gupta, R.B., *Hydrogen fuel: production, transport, and storage*. 2008: CRC press.
26. Ross, D., *Hydrogen storage: the major technological barrier to the development of hydrogen fuel cell cars.* Vacuum, 2006. **80**(10): p. 1084-1089.
27. McCarty, R.D., J. Hord, and H.M. Roder, *Selected properties of hydrogen (engineering design data)*. Vol. 168. 1981: US Department of Commerce, National Bureau of Standards.
28. McCarty, R.D., K.E. Cox, and K. Williamson, *Hydrogen: Its Technology and Implications: Hydrogen Properties*. 2019: CRC Press.
29. Legasov, V., et al., *Nuclear-hydrogen power (prognosis of its devel-opment).* Vopr. At. Nauk. Tekh., Ser. At.-Vodorod. Énerget., 1976. **1**: p. 5-34.
30. Koroneos, C., et al., *Life cycle assessment of hydrogen fuel production processes.* International journal of hydrogen energy, 2004. **29**(14): p. 1443-1450.
31. Rostrup-Nielsen, J.R. and T. Rostrup-Nielsen, *Large-scale hydrogen production.* Cattech, 2002. **6**(4): p. 150-159.
32. Godula-Jopek, A., *Hydrogen production: by electrolysis*. 2015: John Wiley & Sons.
33. Dillich, S., T. Ramsden, and M. Melaina, *Hydrogen production cost using low-cost natural gas.* DOE Hydrogen and Fuel Cells Program Record, 2012. **12024**.
34. Hallenbeck, P.C. and J.R. Benemann, *Biological hydrogen production; fundamentals and limiting processes.* International journal of hydrogen energy, 2002. **27**(11-12): p. 1185-1193.
35. James, B.D., et al., *Technoeconomic analysis of photoelectrochemical (PEC) hydrogen production.* DOE report, 2009.
36. Perret, R., *Solar Thermochemical Hydrogen Production Research (STCH) Thermochemical Cycle Selection and Investment Priority*. 2011, Sandia National Lab.(SNL-CA), Livermore, CA (United States).
37. Saur, G. and C. Ainscough, *US Geographic analysis of the cost of hydrogen from electrolysis*. 2011, National Renewable Energy Lab.(NREL), Golden, CO (United States).
38. Hauch, A., et al., *Highly efficient high temperature electrolysis.* Journal of Materials Chemistry, 2008. **18**(20): p. 2331-2340.
39. Council, H., *Hydrogen Insights–A perspective on hydrogen investment, market development and cost competitiveness.* Hydrogen Council, 2021.
40. Brown, D., *US and World Hydrogen Production—2014.* CryoGas International, 2016. **32**.
41. Cetinkaya, E., I. Dincer, and G.F. Naterer, *Life cycle assessment of various hydrogen production methods.* International journal of hydrogen energy, 2012. **37**(3): p. 2071-2080.
42. de Fátima Palhares, D.D.A., L.G.M. Vieira, and J.J.R. Damasceno, *Hydrogen production by a low-cost electrolyzer developed through the combination of alkaline water electrolysis and solar energy use.* International Journal of Hydrogen Energy, 2018. **43**(9): p. 4265-4275.
43. Ogawa, T., M. Takeuchi, and Y. Kajikawa, *Analysis of trends and emerging technologies in water electrolysis research based on a computational method: a comparison with fuel cell research.* Sustainability, 2018. **10**(2): p. 478.
44. Hauch, A., et al., *Recent advances in solid oxide cell technology for electrolysis.* Science, 2020. **370**(6513): p. eaba6118.
45. David, M., C. Ocampo-Martínez, and R. Sánchez-Peña, *Advances in alkaline water electrolyzers: A review.* Journal of Energy Storage, 2019. **23**: p. 392-403.
46. Ayers, K., *The potential of proton exchange membrane–based electrolysis technology.* Current Opinion in Electrochemistry, 2019. **18**: p. 9-15.
47. Sharifian, S., N. Asasian Kolur, and M. Harasek, *Transient simulation and modeling of photovoltaic-PEM water electrolysis.* Energy Sources, Part A: Recovery, Utilization, and Environmental Effects, 2020. **42**(9): p. 1097-1107.
48. AlZahrani, A.A. and I. Dincer, *Modeling and performance optimization of a solid oxide electrolysis system for hydrogen production.* Applied Energy, 2018. **225**: p. 471-485.

49. Lim, A., et al., *A study on electrode fabrication and operation variables affecting the performance of anion exchange membrane water electrolysis.* Journal of Industrial and Engineering Chemistry, 2019. **76**: p. 410-418.
50. Babic, U., et al., *Critical review—identifying critical gaps for polymer electrolyte water electrolysis development.* Journal of The Electrochemical Society, 2017. **164**(4): p. F387.
51. Millet, P. and S. Grigoriev, *Water electrolysis technologies.* Renewable Hydrogen Technologies: Production, Purification, Storage, Applications and Safety, 2013: p. 19-41.
52. Amores, E., et al., *Development of an operation strategy for hydrogen production using solar PV energy based on fluid dynamic aspects.* Open Engineering, 2017. **7**(1): p. 141-152.
53. Liu, X., et al., *Improving the HER activity of Ni3FeN to convert the superior OER electrocatalyst to an efficient bifunctional electrocatalyst for overall water splitting by doping with molybdenum.* Electrochimica Acta, 2020. **333**: p. 135488.
54. Kamaroddin, M.F.A., N. Sabli, and T.A.T. Abdullah, *Hydrogen production by membrane water splitting technologies.* Advances In Hydrogen Generation Technologies, 2018: p. 19-37.
55. Henkensmeier, D., et al., *Overview: State-of-the art commercial membranes for anion exchange membrane water electrolysis.* Journal of Electrochemical Energy Conversion and Storage, 2021. **18**(2).
56. Ge, Z., et al., *A review of the electrocatalysts on hydrogen evolution reaction with an emphasis on Fe, Co and Ni-based phosphides.* Journal of Materials Science, 2020. **55**(29): p. 14081-14104.
57. Gutić, S.J., et al., *Hydrogen evolution reaction-from single crystal to single atom catalysts.* Catalysts, 2020. **10**(3): p. 290.
58. Haber, J.A., et al., *Multiphase nanostructure of a quinary metal oxide electrocatalyst reveals a new direction for OER electrocatalyst design.* Advanced Energy Materials, 2015. **5**(10): p. 1402307.
59. Holladay, J.D., et al., *An overview of hydrogen production technologies.* Catalysis today, 2009. **139**(4): p. 244-260.
60. Hall, D., *Electrodes for alkaline water electrolysis.* Journal of the Electrochemical Society, 1981. **128**(4): p. 740.
61. Bowen, C., et al., *Developments in advanced alkaline water electrolysis.* International journal of hydrogen energy, 1984. **9**(1-2): p. 59-66.
62. Janjua, M. and R. Le Roy, *Electrocatalyst performance in industrial water electrolysers.* International Journal of Hydrogen Energy, 1985. **10**(1): p. 11-19.
63. Arole, V. and S. Munde, *Fabrication of nanomaterials by top-down and bottom-up approaches-an overview.* J. Mater. Sci, 2014. **1**: p. 89-93.
64. He, B.B., *Two-dimensional X-ray diffraction*. 2018: John Wiley & Sons.
65. Naderi, M., *Surface area: brunauer–emmett–teller (BET)*, in *Progress in filtration and separation*. 2015, Elsevier. p. 585-608.
66. Orazem, M.E. and B. Tribollet, *Electrochemical impedance spectroscopy.* Angew. Chem. Int. Ed, 2009. **48**: p. 1532-1534.
67. He, Z. and F. Mansfeld, *Exploring the use of electrochemical impedance spectroscopy (EIS) in microbial fuel cell studies.* Energy & Environmental Science, 2009. **2**(2): p. 215-219.
68. Cossar, E., et al., *Comparison of electrochemical active surface area methods for various nickel nanostructures.* Journal of Electroanalytical Chemistry, 2020. **870**: p. 114246.
69. Kim, T., et al., *Applications of voltammetry in lithium ion battery research.* Journal of Electrochemical Science and Technology, 2020. **11**(1): p. 14-25.
70. Wei, C., et al., *Approaches for measuring the surface areas of metal oxide electrocatalysts for determining their intrinsic electrocatalytic activity.* Chemical Society Reviews, 2019. **48**(9): p. 2518-2534.

71. Maximilian Schalenbach, O. K. (2018). An alkaline water electrolyzer with nickel electrodes enables efficient high current density operation,. *International Journal of Hydrogen Energy, 43*(27), 11932-11938. Retrieved from https://doi.org/10.1016/j.ijhydene.2018.04.219.

72. Enapter. (2022, September 9). *AEM Electrolyser*. Retrieved from Enapter: https://www.enapter.com/aem-electrolyser

73. Turkevich, J. (1985). Colloidal gold. Part 1. *Gol Bulletin*, 86-91.

74. Dennis A. Corrigan 1987 *J. Electrochem. Soc.* **134** 377

75. Hamid Reza Zamanizadeh, S. S. (2022, August). Tailoring the oxide surface composition of stainless steel for improved OER performance in alkaline water electrolysis. *Electrochimica Acta, 424*, 140561.

76. hystar. (2022, October 19). Products. Retrieved from hystar.com: https://hystar.com/solutions/products/#orion

77. Zamaizadeh, Hamid Reza. PhD Thesis. Cost-effective electrodes for alkaline water electrolyzer. 2022.16. NTNU Open

78. Juchan Yang, Myeong Je Jang, Xiaojun Zeng, Yoo Sei Park, Jooyoung Lee, Sung Mook Choi, Yadong Yin, Non-precious electrocatalysts for oxygen evolution reaction in anion exchange membrane water electrolysis: A mini review, Electrochemistry Communications, Volume 131, 2021, 107118

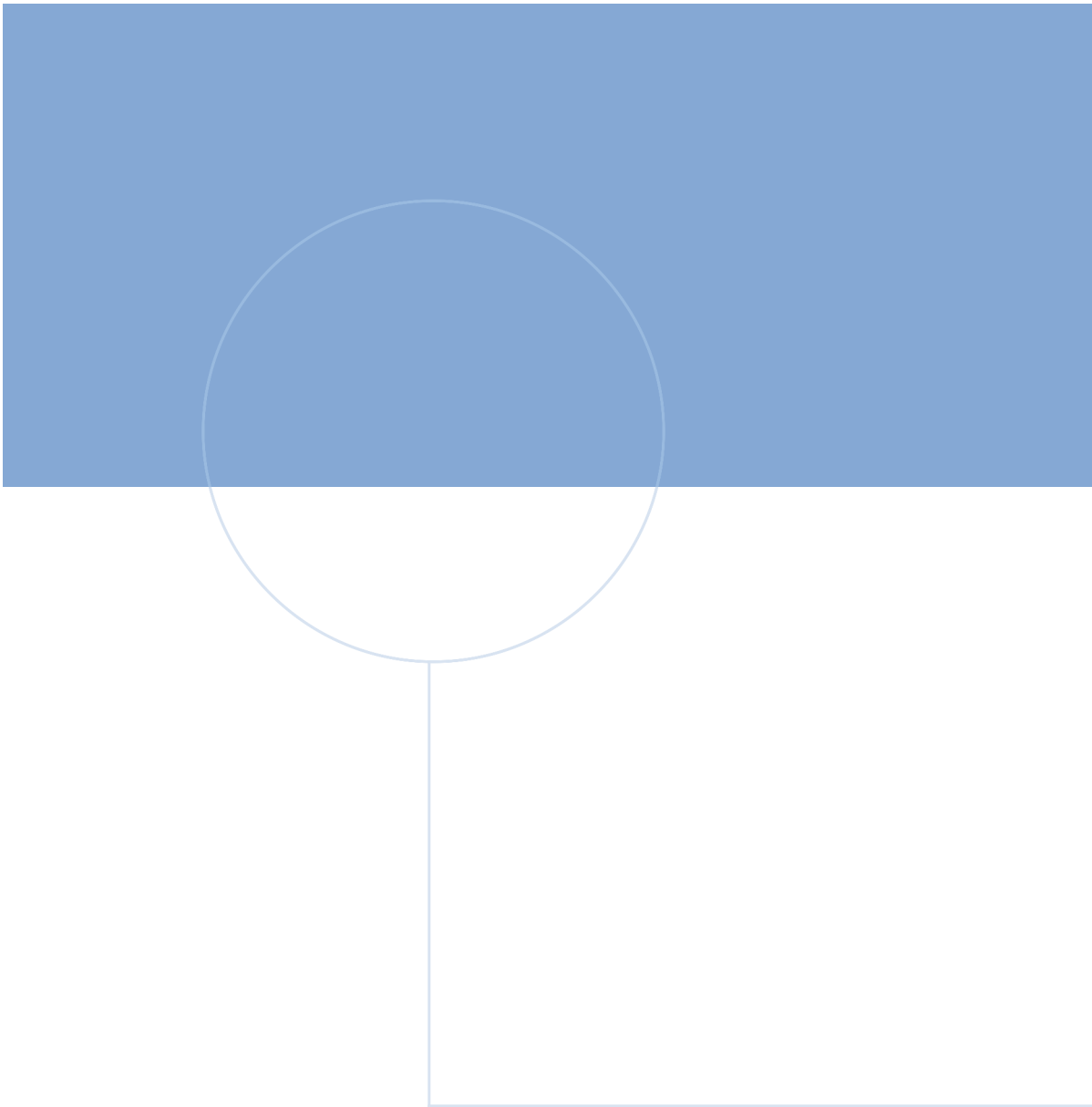

NTNU

Norwegian University of
Science and Technology